ABSTRACT

Title of thesis: QUANTIFICATION OF FLAME HEAT FEEDBACK IN CONE CALORIMETRY TESTS

Jessica Lara Tilles, Master of Science, 2017

Thesis directed by: Associate Professor Dr. Stanislav Stoliarov
Department of Fire Protection Engineering

In order to understand material flammability, accurate pyrolysis models must be developed. Understanding flame heat feedback is essential in developing accurate pyrolysis models. The most widely used standard to quantitatively assess material flammability is the cone calorimeter. The goal of this project was to develop a spatially-resolved flame heat feedback model for 10 cm square horizontal specimens under buoyancy-driven flames to represent the conditions of the cone calorimeter and reasonably, the Fire Propagation Apparatus (FPA). Standard cone calorimeter experiments were performed on several thermoplastics in order to obtain heat release rate (HRR) and mass loss rate (MLR) data. In addition to standard cone calorimetry, side and center flame heat flux was measured under the cone calorimeter using two water-cooled heat flux gauges. The heat flux results show relatively good agreement with prior studies. Heat transfer coefficients were developed from the heat flux measurements in order to quantify heat feedback. It was found that the heat flux in the center of the burning materials is dominated by radiation and the side is dominated by convection. A two-zone heat feedback model with one con-

vection and one radiation dominated zone was then developed, using a heat transfer correlation from the literature. The heat feedback model developed in this study will later be implemented into an in-house numerical pyrolysis model, ThermaKin.

QUANTIFICATION OF FLAME HEAT FEEDBACK IN CONE CALORIMETRY TESTS

by

Jessica Lara Tilles

Thesis submitted to the Faculty of the Graduate School of the
University of Maryland, College Park in partial fulfillment
of the requirements for the degree of
Master of Science
2017

Advisory Committee:
Associate Professor Stanislav Stoliarov, PhD., Chair
Professor Peter Sunderland, PhD.
Professor Arnaud Trouvé, PhD.

Acknowledgments

First and foremost, I would like to thank my advisor, Dr. Stanislav Stoliarov, for giving me this opportunity to advance my knowledge of fire science. His expertise, work ethic, and attention to detail is inspiring. I am so grateful for all that he has taught me and will take these lessons with me wherever I go.

I would also like to acknowledge the FAA for funding my research. The combination of funds from the FAA and support from the Department of Fire Protection Engineering made this work possible. I am so lucky to have had both financial and personal support from the FPE department throughout my time at Maryland. I would specifically like to thank Nicole Hollywood and Dr. Milke for advising me and giving me research opportunities throughout my undergraduate career which lead me to this point.

It is also important to acknowledge my committee members Dr. Peter Sunderland and Dr. Arnaud Trouvé. As a student, I have learned so much from the both of you. It was an honor to have you both on my committee and receive your feedback on my work.

Additionally, I need to acknowledge my wonderful group members. Thanks to Conor for listening to all my concerns, keeping me entertained in the lab, and continuing on with this project. I would also like to thank Ahmed for keeping me sane when dealing with the cone and spending hours troubleshooting with me when the cone was misbehaving. Thanks to Josh, Yan, and the rest of the group for answering all of my questions and letting me practice my defense for you multiple

times.

Lastly I would like to thank my family for being a constant source of support. Thanks for always encouraging me and believing in me. Without you I would never have made it to this point.

List of Abbreviations

AFM: Advanced Flammability Measurements

ASET: Available Safe Egress Time

CFD: Computational Fluid Dynamics

DAQ: Data Acquisition System

FDS: Fire Dynamic Simulator

FPA: Fire Propagation Apparatus

HF: Heat Flux

HRR: Heat Release Rate

HIPS: High Impact Polystyrene

MLR: Mass Loss Rate

PBT: Polybutylene terephthalate 25% Glasfiber

PBT-GF: 70% PBT 30% Glasfiber

PBT/GF: 75% PBT 25% Glasfiber

PBT/GF/Exolit: 59% PBT 25% Glasfiber 16% Aluminum phosphinate

PMMA: Poly(methyl methacrylate)

POM: Polyoxymethylene

Table of Contents

List of Tables

List of Figures

Chapter 1: Introduction

1.1 Background

Fires are a constant threat to society. Just this June, there have been two major fires in London and Portugal that have caused more than 140 fatalities combined [6] [7]. The Grenfell Tower building in London was fitted with Reynobond PE (flammable cladding with a plastic core) with a 2 inch cavity between the cladding and flammable insulation. The cladding and insulation caught fire. The air from the cavity and the radiant heat from the burning materials allowed the fire to spread rapidly. While this material is banned from use on high-rises in the U.S., it was legal in London [6].

Knowledge of material flammability is essential in the practice of fire protection. Understanding the fire hazard of the flammable cladding used in Grenfell Tower enabled U.S. regulators to ban the use of Reynobond PE in high-rises. Studying material flammability helps us to classify materials, understand the fire hazard of materials, and develop standards and codes to help protect people from fire hazards.

1.2 Literature Review

1.2.1 Methods to Quantify Fire Hazards

Flammability describes how a material reacts to heat or flames. Quantities such as heat release rate (HRR), toxicity of combustion products, time to ignition, and flame spread rate are of great interest in the study of material flammability. Most fatalities from fires are a direct result of smoke inhalation; consequently, in the 1970s, interest in the toxicity of materials grew. Research in toxicity led to the development of Available Safe Egress Time (ASET) [8]. ASET is used in enclosure fires to measure the amount of time from fire inception to the point when a space becomes untenable. While toxicity contributes, fire size is a more significant factor in determining ASET and understanding materials' hazards to life safety [9]. Thus, the most instrumental parameter in determining fire hazard is understanding the fire size. HRR is a way to quantify the size of fires and thus the hazard that they pose. It is also the key quantity which can link bench-scale tests to accurately represent full-scale fire scenarios. A study by Babrauskas and Peacock in 1992 compared the flammability properties of HRR, ignition time, and material toxicity. They found that increasing the HRR was the only factor that lead to a significant decrease in tenability time [8].

Historically, HRR was calculated based on temperature measurements of the heat released during the combustion reaction. This method required extensive sensors and measurements and did not produce accurate results [10]. When a combus-

tion reaction occurs, heat is released and oxygen is consumed proportionally. Thus, an alternative method to measure HRR is through oxygen consumption measurements. The cone calorimeter was developed in 1984 to measure HRR based on this principle [11].

Oxygen consumption depends on heat of combustion (Δh_c), the stochiometric oxygen to fuel mass ratio (r_0), and the mass flow rate of oxygen ($\dot{m}_{O_2}$). HRR, or $\dot{q}$ is calculated using the equation below.

$$\dot{q} = (\frac{\Delta h_c}{r_0})(\dot{m}_{O_2,\infty} - \dot{m}_{O_2}) \tag{1.1}$$

In 1980, Huggett refined the concept of oxygen consumption calorimetry to measure HRR. He found that the heat of combustion per kg oxygen consumed ($\Delta h_c/r_0$) is a constant value of 13.1×10^3 kJ/kg among many different fuels [10]. This finding greatly simplified the method of finding HRR as only the mass flow rate of oxygen is required.

The ASTM E1354 standard provides guidance on the operation of the cone calorimeter and has been found to produce reliable and reproducible measurements under controlled conditions and can be used to represent full-scale fire scenarios. Gram-scale samples can be tested under various radiant heat fluxes in either vertical or horizontal configurations [12] [11].

Another essential device in the study of materials subjected to external heat fluxes is the fire propagation apparatus (FPA). The FPA can be used in accordance with the ASTM E2058 standard to measure ignition time, heat release rate

(HRR), and mass loss rate (MLR), to name a few quantities [13]. Similarly to the cone calorimeter, the knowledge of these flammability properties gained from FPA experiments can be used to model burning behavior for full-scale scenarios. The biggest difference between the cone calorimeter and the FPA is that the atmosphere of the FPA can be controlled, while the standard cone calorimeter lacks this ability. Additionally, as the name suggests, the cone uses an electrical conical heater positioned directly above the sample. The FPA instead uses infrared tungsten lamps placed on the side of the apparatus [14].

There are some other differences in the geometry of the apparatuses including the methods to pilot ignition. A spark is used as the pilot for the cone while the FPA uses an air/ethylene flame to pilot ignition. Although these physical differences have some effect on the results, both the cone and the FPA produce comparable material flammability measurements [14]. The cone is used much more readily than the FPA, and thus was chosen as the apparatus for this project.

1.2.2 Attempts to Model Heat Flux to the Surface

Fire tests can provide empirical knowledge of material flammability, but can be expensive and time-consuming; therefore, numerical models are desired. A one-dimensional model characterizing charring, vaporization, extinction, and conduction effects was first developed by Quintiere in 1992. Later, Quintiere and Iqbal created a model that also produces results for unsteady burning rates. The model designed by Quintiere and Iqbal uses an integral method to model the gasification of a ther-

moplastic, but did not consider flame effects. Iqbal later expanded the model to include the flame effects of radiation and convection from laminar and turbulent flames. It was found that radiation from the flame is a principal factor in burning rate, specifically for turbulent flames. At the time, there was no rigorous approach to predicting flame radiation and burning rate. In order to develop accurate models to predict burning rate of materials, it is critical to understand the flame heat flux at the material surface. [15].

In 1996, Rhodes and Quintiere sought to develop a model of surface heat flux, including flame effects, for the cone calorimeter. The two performed cone calorimeter experiments with 25 mm thick black Poly(methyl methacrylate) (PMMA) where they measured mass loss, heat flux, and surface temperature. The surface heat flux was measured with a heat flux gauge in the center of the sample. Due to monomer deposits on the heat flux gauge during experiments, Rhodes and Quintiere were not able to obtain accurate heat flux measurements from their experiments. Instead, the two used the ignition and burning rate information from their experiments to obtain material properties. Those material properties were then used in a heat transfer analysis to model flame heat flux with both radiative and convective components. It was found that the total flame heat flux could be modeled as a constant, which for black PMMA was approximately 37 kW/m^2. Because no accurate heat flux data was obtained from the cone calorimeter experiments, Rhodes and Quintiere used a methane burner to simulate PMMA burning, and measured the heat flux to be a constant 27 kW/m^2. The methane burner experiments were used to experimentally confirm that heat flux could be measured as a constant [15]. The simple model

developed by Rhodes and Quintere marked the beginning of more in-depth surface heat flux measurements.

The burning of black PMMA under the cone calorimeter was further examined in a 2005 study by Linteris et al. Both vertical and horizontal configurations of 10 cm square, 2.5 cm thick samples of black PMMA were exposed to various radiant heat fluxes ranging from 0 to 75 kW/m^2. Visual observations, HRR, and MLR were recorded. Heat Flux was determined from the MLR results and then used to model burning rate in a computational fluid dynamics (CFD) fire model. It was found that burning rate was inconsistent over the surface of the sample, particularly for samples exposed to lower external heat fluxes [16]. The erratic burning behavior represented a need to further research flame heat feedback and characterize burning rate.

In the early 2000s, researchers hypothesized that small scale tests with increased ambient oxygen can produce larger heat fluxes that resemble those found in large-scale well ventilated fires. Because there had not been sufficient experiments done to quantify the increased heat flux, in 2006, Beaulieu and Dembsey studied the effect of oxygen concentration on flame heat flux for bench scale tests. Later, they sought to develop its relationship to large-scale fire scenarios. Black PMMA and POM were tested with the Advanced Flammability Measurements (AFM) Apparatus using ambient oxygen concentrations ranging from 20.9 to 40%. The AFM is similar to the bench scale FPA (ASTM E2058) as well as the cone calorimeter (ASTM E1354), except that the AFM can be used to conduct larger, intermediate scale tests [1]. In the AFM, total flame heat flux was measured with Schmidt-Boelter

heat flux gauges of varying diameters, in the center of the samples. The flame height, temperature, and emissivity were also measured to help calculate the radiative and convective heat flux components, in addition to understanding the effects of oxygen. The measured heat flux results from Beaulieu and Dembsey's horizontal orientation small scale tests are shown below in table 1.1 [1]. From these experiments, Beaulieu and Dembsey concluded that the increased oxygen concentration causes the flame temperature to rise, which then increases the rate of the chemical reactions [1].

Table 1.1: Heat Flux Measurements from Beaulieu and Dembsey [1]

Material		20.9% Oxygen	40% Oxygen
Black PMMA	Radiative	12 ± 3	20 ± 3
	Convective	8 ± 3	10 ± 3
	Total	20 ± 3	30 ± 3
Black POM	Radiative	0 ± 3	3 ± 3
	Convective	11 ± 3	30 ± 3
	Total	11 ± 3	33 ± 3

As knowledge of material properties and surface heat flux grew, comprehensive pyrolysis models were being developed. One of the first advanced pyrolysis models was developed in 2008 by Stoliarov and Lyon. The two developed a one-dimensional C++ thermo-kinetic model called ThermaKin to predict fire behavior of materials exposed to external heat fluxes. At a low computational cost, ThermaKin analyzes the chemistry and thermal transport of pyrolyzing materials. The simulation is run

after inputting temperature-dependent material properties including density, heat capacity, thermal conductivity, and gas transfer coefficient [17].

A 2009 study by Stoliarov et al. investigated if pyrolysis models can be used to accurately predict the results of fire calorimetry tests. Non-charring polymers including PMMA, high-impact polystyrene (HIPS), and high-density polyethylene (HDP) were examined in this project. Initially the material properties of these materials were gathered from literature or measured to provide accurate material characterization for the model. Gasification experiments were performed in addition to cone calorimeter experiments which were executed under a wide range of external heat fluxes and sample thicknesses [18]. The HRR from the cone calorimeter experiments was used in conjunction with the model to determine the heat flux from the flame. A first order model for heat flux was made by compiling results from Beaulieu and Dembsey's study and using a mean value of 16 kW/m^2 to model incident heat flux. It was found that the pyrolysis model gives rational predictions of MLR, HRR, and temperature change within the materials. It has limited accuracy in predicting ignition time at different heat fluxes and does not perform well at low heat fluxes [18].

Another study that was performed in order to verify the predictive capabilities of ThermaKin was done by Kempel et al. in 2012. This study focused on the ability of numerical simulation tools to predict mass loss rate for polymers that form residue. One material without significant residue formation, Polybutylene terephthalate (PBT), and one material with significant residue formation, PBT with 30% glasfiber (PBT-GF), was selected for the 2012 study. Gasification and

cone calorimeter experiments were performed with 4 mm thick samples of PBT and PBT-GF. The gasification experiments were conducted with 75 mm diameter samples under an external heat flux of 50 kW/m^2. The cone calorimeter experiments were conducted with 10 cm square samples under external heat fluxes ranging from 35 to 70 kW/m^2, with a Schmidt-Boelter heat flux gauge in the center of the sample to measure total heat flux to the sample [19].

Total heat flux to the surface was found to be constant for each material at each external heat flux from the experiments. The constant surface heat flux was used in Fire Dynamic Simulator (FDS) and ThermaKin to model mass loss for the two materials tested. It was found that both models produced accurate results for the MLR of PBT; however, it was found that both models had limited capability in predicting MLR for PBT-GF for the cone calorimeter experiments [19].

In order to improve ThermaKin's predictive abilities, in 2015, Leventon et al. measured heat flux and mass loss on PMMA samples ranging in heights from 3 to 20 cm that were subjected to upward flame spread. This data was compiled to create a height-dependent empirical heat feedback model [2]. This heat feedback model was combined with ThermaKin2D which is an updated version of the computational pyrolysis model ThermaKin. The model was developed by Stoliarov and Lyon using information from both milligram-scale thermal analysis and gram-scale gasification experiments. ThermaKin2D utilizes material properties to solve conservation equations and calculate the transient gaseous fuel production rate of pyrolyzing materials. The findings produced by Leventon et al. improved the pre-existing wall flame model to more accurately predict ignition, vertical burning, and

upward flame spread [2].

Similar to the Leventon et al. study, in 2016 Kacem et al. developed a heat feedback model for PMMA, but for horizontal orientation instead of vertical. Kacem et al. tested 3 cm thick PMMA samples ranging in size from 10 cm squares to 40 cm squares by burning them in open air. Total heat flux was measured with a Medtherm heat flux gauge threaded through a hole in the center of the PMMA sample. The radiative portion of the heat flux was found using a zinc-selenide lens on top of the heat flux gauge. The convective portion of the heat flux was determined by subtracting the radiative portion from the total measured heat flux. It was found that total heat flux increases with increased sample size; however, the percentage of radiative heat flux remained constant at around 80% [20].

In 2017 Leventon et al. expanded on the heat feedback model for PMMA by measuring upward flame spread characteristics on seven prevalent polymers. Flame height is essential in modeling heat transfer for vertical flame spread. In the previous PMMA flame model, flame height was defined in terms of the distance from the flame base to the height of the highest measured heat flux [2]. It has been determined that flame height is reliant on HRR, and therefore is linked to heat of combustion. The new model uses the heat of combustion of the tested material in ratio with the heat of combustion of extruded PMMA to get the heat flux flame height. The heat of combustion for each polymer tested in this study was found through experiments in a milligram-scale combustion calorimeter [4].

The new flame heat flux model developed in 2017 accurately matches experimental measurements for all seven polymers tested within 3.8 kW/m^2 which is

within two standard deviations of the mean. The heat flux model, when coupled with the pyrolysis model ThermaKin2D, enables accurate predictions of ignition and flame spread for a wide range of fire scenarios at a relatively low computational cost [4].

Pyrolysis models such as ThermaKin function on the process of analyzing the three key processes in pyrolysis: heat transfer, mass transfer, and the thermokinetics behind thermal degradation. These models can stand alone or be combined with CFD fire codes. The French Institute of Radioprotection and Nuclear Safety (IRSN) developed their own three-dimensional CFD fire model called ISIS [21]. In 2017, Boyer developed a pyrolysis model similar to the preceding models, which can be combined with IRSN ISIS fire simulation software. Boyer's model can also be used alone with some heat transfer assumptions representative of cone calorimeter experiments [3].

Boyer's program requires extensive material parameters to be inputted, and therefore a deeper understanding of physical properties is necessary. This entails characterizing thermal, radiative, and thermokinetic properties as well as understanding pyrolysis and soot products involved in the process of burning materials. The results from gasification and cone calorimeter experiments performed by Stoliarov et. al were compared to the stand alone pyrolysis model and the pyrolysis model coupled with the ISIS CFD model respectively. The mass loss rate (MLR) from the gasification experiments and the HRR per unit area from the cone calorimeter experiments were found to be closely consistent with the model [3].

In an effort to further validate existing CFD models, another study with IRSN

was performed in 2017. Alibert et al. worked to test 3 cm thick, 20 cm square horizontally-oriented samples of PMMA in a controlled atmosphere calorimeter, CADUCEE, to investigate the effects of varying oxygen concentrations. Heat flux sensors, or radiometers, were threaded through holes drilled in the center of the PMMA samples in order to measure total heat flux and radiative heat flux to the surface of the sample respectively. Convective heat flux was calculated by taking the difference between the radiative and total heat fluxes. It was found that heat flux and MLR decrease as oxygen concentration decreases. The changing oxygen concentrations were not found to affect the ratio of radiatve and convective portions of the heat flux to the surface, which remain at 65% and 35% respectively [22].

1.3 Purpose

Currently, flame heat feedback for horizontal pyrolysing solids under the cone calorimeter is not fully understood. Measuring heat flux on the surface of the burning samples is a good way to learn about flame heat feedback. This information can be utilized in pyrolysis models to more accurately predict burning rate and material flammability. Most simulations model heat flux as a constant throughout the surface of the material.

The purpose of this research is to improve our understanding of flame heat feedback across the surface of a horizontal burning material. The surface heat flux of thermoplastics were tested on the side and center of samples under the cone calorimeter. This information is then analyzed and a new and improved model for

flame heat feedback is developed. This model will then be added to ThermaKin to improve its accuracy in predicting material burning.

Chapter 2: Methodology

2.1 Experimental Setup

Both standard and non-standard experiments were conducted in this project using a Govmark cone calorimeter. The standard experiments were done in accordance with the ASTM E1354 standard in order to collect HRR and MLR data [12]. The non-standard, double heat flux gauge experiments were modified from the standard in order to take heat flux measurements on the surface of the samples.

2.1.1 Standard Cone Calorimeter Experiments

Before the standard cone calorimeter experiments were conducted, all filters, drierite, and ascarite on the cone calorimeter were checked and replaced if needed. The thermocouples, pressure transducer, and O-ring were cleaned after burning highly sooting samples. The gas analyzers, load cell, and methane calibration were performed daily.

Prior to testing, the sample's surface area was measured with a digital caliper and then wrapped in foil on five sides. The sample and foil were then weighed on a separate scale. The sample holder for the cone calorimeter experiments was stacked

with three pieces of 6.35 mm Kaowool PM and a 100 mm square foil-wrapped sample, which can be seen in figure 2.1. The properties for the Kaowool PM can be seen below in table 2.1

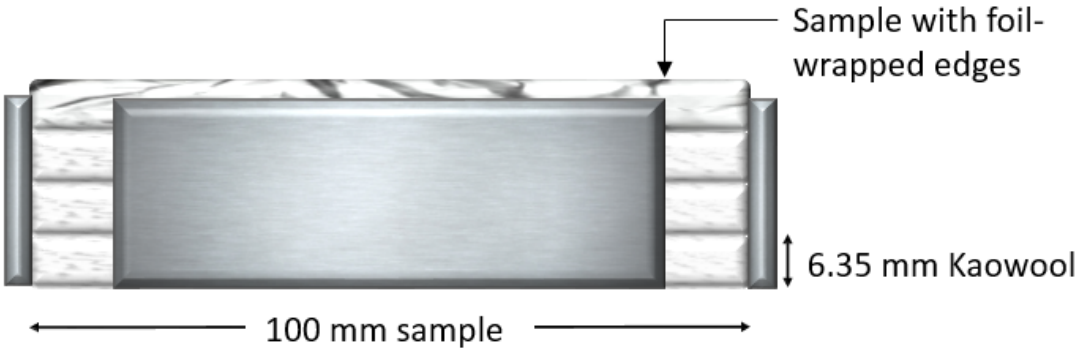

Figure 2.1: Side-View Diagram of Experiments

Table 2.1: Kaowool PM Properties [2]

Property	Symbol	Value
Density	$\rho[kg/m^3]$	256
Specific Heat	c [kJ/kg-K]	1.07
Radiation Absorption Coefficient	$\alpha[m^2/\text{kg}]$	1×10^3 (non-transparent)
Thermal Conductivity	k [W/m-K]	$5.2\text{-}4\times10^{-}7T+1\times10^{-}7T^2$

While the sample was being prepared, the external heat flux was set on the heater using the cone calorimeter's heat flux gauge. The surface of the sample was then placed 25.4 mm below the bottom of the conical heater with the support of the sample holder assembly. After each experiment was completed and the sample was allowed to cool, the foil and remaining sample were weighed. These tests were preformed daily on black PMMA before any sample material was tested. The heat of combustion from the black PMMA experiment was compared to the standard value

of 25 kJ/g in order to confirm that the cone calorimeter was calibrated properly.

After conducting some initial experiments, it was discovered that POM had a tendency to swell and rise from the foil wrapping under the cone. The swelling could lead to inaccurate results because it could interfere with ignition times and cause uneven heating. To combat this problem, epoxy was used to adhere the POM to the foil and then adhere the foil to an additional layer of foil which was wrapped around the top layer of Kaowool PM insulation. The cone tests for POM at 20.6 kW/m^2 were re-done with the epoxy as well as one test for POM at 51.5 kW/m^2 these are labeled as "glued test".

2.1.2 Double Heat Flux Gauge Experiments

The other type of experiments conducted, double heat flux gauge experiments, included a 100 mm square sample in a 110 mm square sample holder. The sample holder has one hole in the center and one in the side so that two Medtherm water-cooled heat flux gauges could be threaded through the holder. A top view diagram of the sample and holder can be seen in diagram 2.2

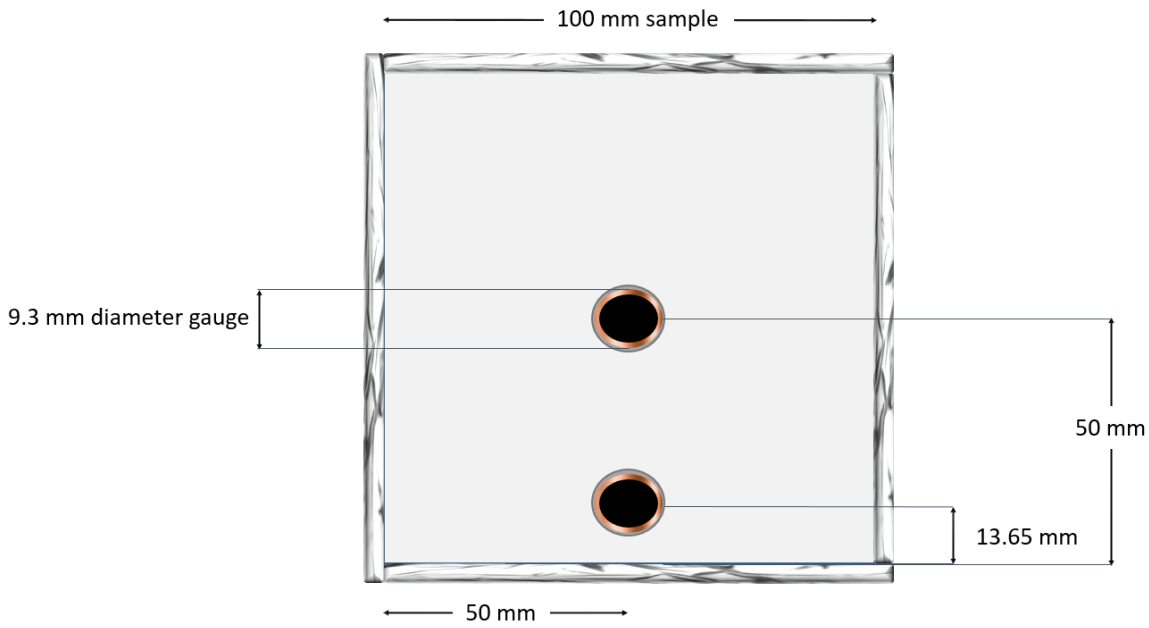

Figure 2.2: Top-View Diagram of Double Heat Flux Gauge Experiments

Two 9.6 mm holes were drilled in every sample 13.65 mm and 50 mm from the edge as shown in diagram 2.2. Each material tested was then dried for at least 48 hours prior to testing in a dessicator with drierite. Before the experiment, the sample was removed from the dessicator and wrapped in extra heavy duty aluminum foil with holes removed for the gauges.

Prior to every experiment, the 9.3 mm water-cooled Medtherm heat flux gauges were painted and calibrated. Medtherm High Temperature Optical Black Coating with emissivity of 0.94 was used to paint the gauges. The gauges were then individually calibrated under the cone calorimeter heater against the cone heat flux gauge and new calibration coefficients were determined. Gauge temperature was held constant by flowing cool water at 291 K.

Once the gauges were calibrated, the heater on the cone was set to either 20.6

or 51.5 kW/m^2, using the cone calorimeter heat flux gauge and the CC1 software. While the cone calorimeter heat flux was being set, the gauges were threaded through the sample holder, the three pieces of Kaowool PM insulation, the foil, and the sample. Both gauges were placed approximately 2 mm above the surface of the sample in order to accommodate for swelling of the sample. A section view of this setup can be seen in figure 2.3. During the calibration process, a video camera is set up on a tripod in front of the cone to record the experiments.

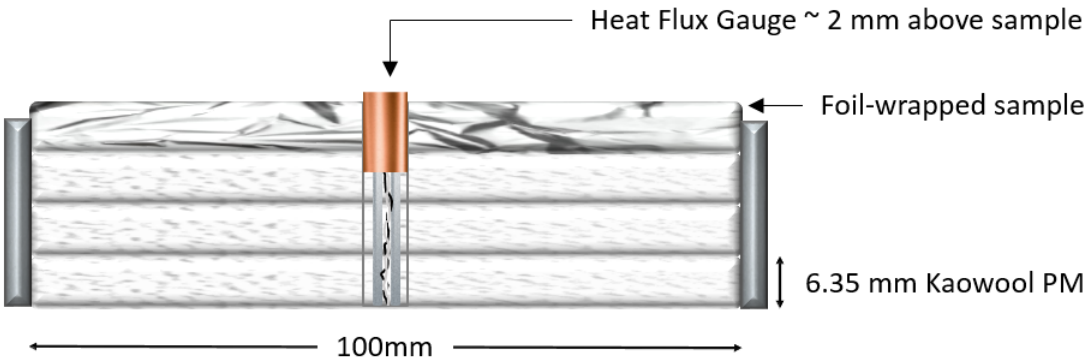

Figure 2.3: Section-View Diagram of Double Heat Flux Gauge Experiments

After the heat flux on the cone was set, the shutter on the cone was closed to prevent pre-heatingof the sample. The heat flux gauges were then connected to a data acquisition system (DAQ) which was connected to a computer running Labview. The Labview program records voltage data and simultaneously converts it to heat flux with the calibration coefficients found earlier.

Once the gauges were connected to the DAQ, the sample holder apparatus was placed under the cone and the cone exhaust was turned on. A stopwatch was started simultaneously with the video camera. Next, the DAQ recording was initiated and the time when recording began was documented. Once the recording was initiated,

the shutter was opened, and the spark igniter was put in place. This time was documented as the starting time of the experiment. The spark igniter was placed slightly off center so as to prevent arcing with the gauges. When ignition occurred, the time was recorded and the spark igniter was removed. Extinction time was also recorded at the time when burning ceased.

2.1.2.1 Additional Tests

The swelling behavior that was discovered for the POM would cause the material surface to move away from the gauges, which would interfere with surface measurements. To combat this problem and maintain consistency with the cone calorimeter tests, epoxy was used for all of the POM double heat flux gauge experiments.

For PMMA and HIPS at 20.6 kW/m^2, "covered gauge" tests were performed in order to understand if the gauges were affected by soot deposits. These tests entailed covering the heat flux gauges with pieces of copper tube stuffed with glasfiber and and attached to a long piece of Kanthal wire as seen in figure 2.4. These covers were removed using tongs about 150 s after ignition.

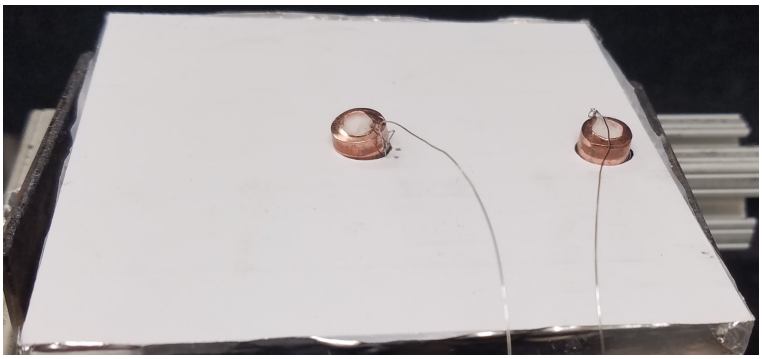

Figure 2.4: Covered Gauge Test

In order to understand the effect (if any) of edges on heat flux measurements, one "extended edges" test was conducted for PMMA at 51.5 kW/m^2. The PMMA samples were 6 mm thick and foil was wrapped around the 6 mm edges and the bottom of the samples. For the "extended edges" test, the foil surrounding the edges of the sample was increased to 9 mm in height instead of 6 mm in height to simulate extended edges.

2.2 Material Specifications and Test Matrix

The materials used in this project include Polyoxymethylene (POM), Poly(methyl methacrylate) (PMMA), High Impact Polystyrene (HIPS), and Polybutylene terephthalate (PBT) with Glasfiber. These materials were chosen so as to have a wide range of thermoplastics from the ideal almost complete combustion of POM, to the highly sooting incomplete combustion of HIPS and PBT. The PBT with glasfiber came in two forms: with and without flame retardant (Exolit). The PBT/GF consists of 75% Ultradur B4500 (PBT Brand) and 25% Glasfiber PPG 3786. The PBT/GF/Exolit consists of consists of 59% Ultradur B4500 (PBT Brand), 25% Glasfiber PPG 3786, and 16% Exolit OP 1240. The manufacturers and distributors for these materials can be seen in table 2.2.

Table 2.2: Material Specifications

Polymer Name	Thickness [mm]	Color	Manufacturer	Distributor
Polyoxymethylene **(POM)**	6.35	White	Ensinger	Curbell Plastics
Poly(methyl methacrylate) **(PMMA)**	6	Clear	Evonik Industries	US Plastics
High Impact Polystyrene **(HIPS)**	6	White	Spartech Plastics	Professional Plastics
Polybutylene terephthalate **(PBT/GF)**	5.6	White	BASF	BASF
Polybutylene terephthalate **(PBT/GF/Exolit)**	5.6	White	BASF	BASF

The samples were each 100 mm ± 2.5 mm squares. Samples were tested under external heat fluxes of 20.6 and 51.5 kW/m^2 in order to simulate low and high heat flux conditions. Most of the standard cone calorimeter and double heat flux gauge experiments were conducted three times in order to assess repeatability. The POM standard cone calorimeter test was performed a forth time in order to conduct an additional glued test for reasons discussed previously. Both PBT/GF and PBT/GF/Exolit were only tested at the high heat flux, two times instead of three, due to a limited supply of samples. The higher heat flux was favored for the PBT samples because samples tested under the higher heat flux generally produced more repeatable results. Table 2.3 which can be seen below, is a text matrix that shows all the experiments included in this project.

Table 2.3: Test Matrix

Type of Experiment	Material	External Heat Flux [kW/m^2]	Number
Standard Cone Calorimeter	POM	20.6	3
		51.5	4
	PMMA	20.6	3
		51.5	3
	HIPS	20.6	3
		51.5	3
	PBT/GF	51.5	2
	PBT/GF/Exolit	51.5	2
Double Heat Flux Gauge	POM	20.6	3
		51.5	3
	PMMA	20.6	3
		51.5	3
	HIPS	20.6	3
		51.5	2
	PBT/GF	51.5	2
	PBT/GF/Exolit	51.5	2
Covered gauge	PMMA	20.6	1
	HIPS	20.6	1
Extended edges	PMMA	51.5	1
Total			47

Chapter 3: Results

3.1 Cone Calorimeter Measurements

3.1.1 Data Analysis

Heat release rate (HRR) and mass loss rate (MLR) graphs were compiled from the cone calorimeter standard experiments. The HRR graphs were obtained from the raw HRR data whereas the MLR graphs were made by taking a time derivative of the sample mass and normalized by the initial area of the sample. An example of these HRR and MLR graphs can be seen below in figures 3.1 and 3.2 respectively. The raw graphs for the rest of the materials can be seen in the Appendix.

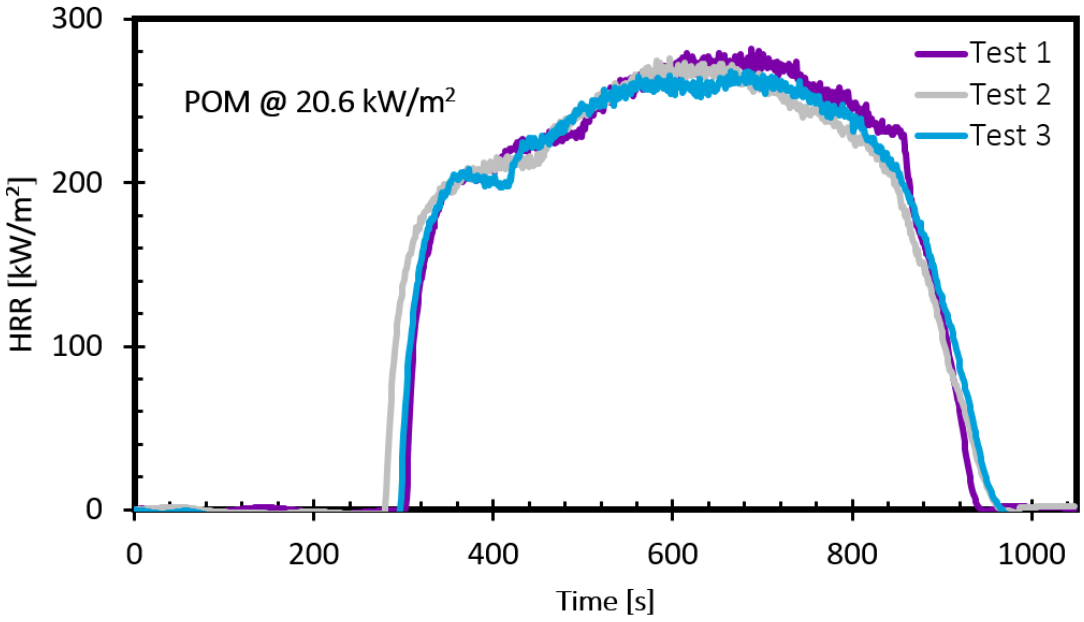

Figure 3.1: Heat Release Rate for POM at 20.6 kW/m^2

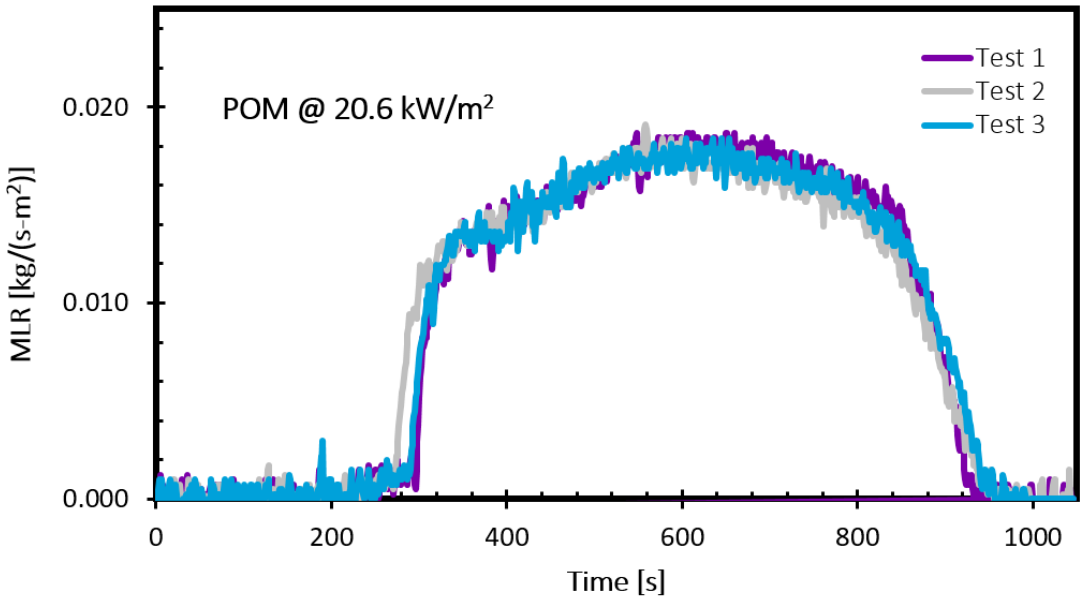

Figure 3.2: Mass Loss Rate for POM at 20.6 kW/m^2

As seen in the graphs above, the cone calorimeter tests were extremely repeat-

able for POM at 20.6 kW/m^2. These graphs also follow the expected behavior for HRR and MLR. This is consistent among all the materials tested, which is why the rest of the HRR and MLR graphs are in the Appendix.

During each standard cone calorimeter experiment, ignition time was recorded from visual observation. These times were then confirmed with the initial spikes in HRR and MLR. It was found that recorded ignition time was relatively consistent with the HRR and MLR data for all experiments. The average of the recorded ignition times for each material at each heat flux was taken and is reported in table 3.1 along with the standard error. Standard error for all values was calculated with equation 3.1, where δ is the standard deviation, and N is the number of points used in the computing the standard deviation and mean. Every time standard error is shown in this project, it was calculated with equation 3.1

$$error = \frac{2\delta}{\sqrt{N}} \tag{3.1}$$

Table 3.1: Average Ignition Time from Cone Calorimeter Tests

Heat Flux [$\mathbf{kW/m^2}$]	Material	Ignition Time [s]
20.6	POM	291.3 ±11.9
	PMMA	221.7 ±15.5
	HIPS	380.3 ±13.8
51.5	POM	44.7 ±1.3
	PMMA	34.0 ±2.3
	HIPS	39.7 ±1.3
	PBT/GF	53.5 ±1.0
	PBT/GF/Exolit	48.5 ±3.0

The total heat released for each cone calorimeter experiment was calculated in kJ by integrating the HRR and multiplying by the initial area of the sample. Two heats of combustion, ΔH_c, were then determined for each experiment based on initial mass and total mass burnt. These values are shown in tables 3.2 and 3.3 with the mean and standard error values for each material.

Table 3.2: Heats of Combustion Derived from Cone Calorimeter Tests

Material	Heat Flux [kW/m^2]	Initial Mass $\Delta H_c[kJ/g]$	Mass Burnt $\Delta H_c[kJ/g]$
POM	20.6	14.9	14.9
		14.9	14.8
		14.8	14.9
	51.5	15.6	15.6
		15.6	15.6
		15.8	15.8
mean with error		15.3 ±0.35	15.3 ±0.34
PMMA	20.6	25.6	25.6
		25.9	25.9
		25.5	25.5
	51.5	25.0	25.0
		25.1	25.1
		25.7	25.7
mean with error		25.5 ±0.28	25.5 ±0.28
HIPS	20.6	30.3	31.6
		30.6	31.9
		31.0	32.3
	51.5	29.3	30.2
		29.6	30.6
		29.7	30.7
mean with error		30.1 ±0.53	31.2 ±0.68

Table 3.3: Heats of Combustion from Cone Calorimeter Tests Continued

Material	Heat Flux [kW/m^2]	Initial Mass $\Delta H_c[kJ/g]$	Mass Burnt $\Delta H_c[kJ/g]$
PBT/GF	51.5	14.8	19.9
		14.8	19.9
mean with error		14.8 $\pm$0.01	19.9 $\pm$0.01
PBT/GF/Exolit	51.5	12.0	18.1
		12.0	18.0
mean with error		12.0 $\pm$0.02	18.1 $\pm$0.04

3.1.2 Visual Observations

It is imperative to analyze the behavior of materials to understand what is happening over the period of time the measurements were taken. In order to enable more thorough observations to be made, every experiment was recorded on video. Picture timelines were then developed from the videos of the cone calorimeter experiments for each material, at each heat flux tested. An example of a picture timeline for POM at 20.6 kW/m^2 can be seen below in figure 3.3. The ignition times noted on the timelines come from the average ignition times between cone calorimeter tests listed in table 3.1.

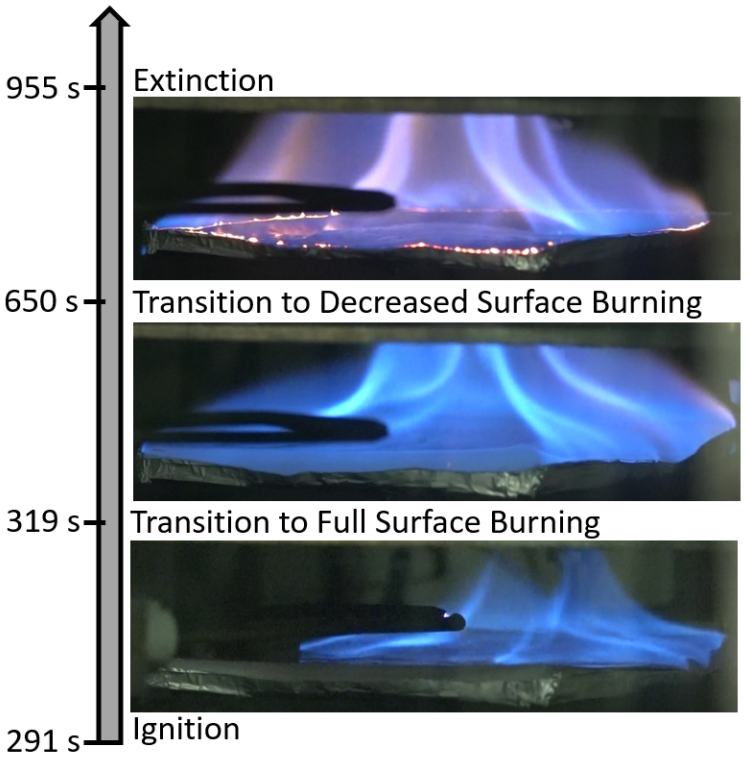

Figure 3.3: Timeline of POM at 20.6 kW/m^2

As seen above in figure 3.3, for POM at 20.6 kW/m^2, ignition began in the center of the material. It then took 28 s for the flames to spread to the edges, or to transition to full surface burning. The top picture in figure 3.3 shows when the surface of the POM diminished and experienced decreased surface burning. Decreased surface burning was defined from visual inspection when the surface of the material receded approximately 3 mm, or half way from the initial thickness. 50% of the area under the HRR curve correlates with half of the area of the sample; therefore, instead of using visual inspection, this decreased surface burning time can be found based on the HRR criteria. This pattern of material recession occurs for POM, PMMA, and HIPS. PBT/GF and PBT/GF/Exolit do not experience a full material recession. An example of this can be seen for PBT/GF in figure 3.4.

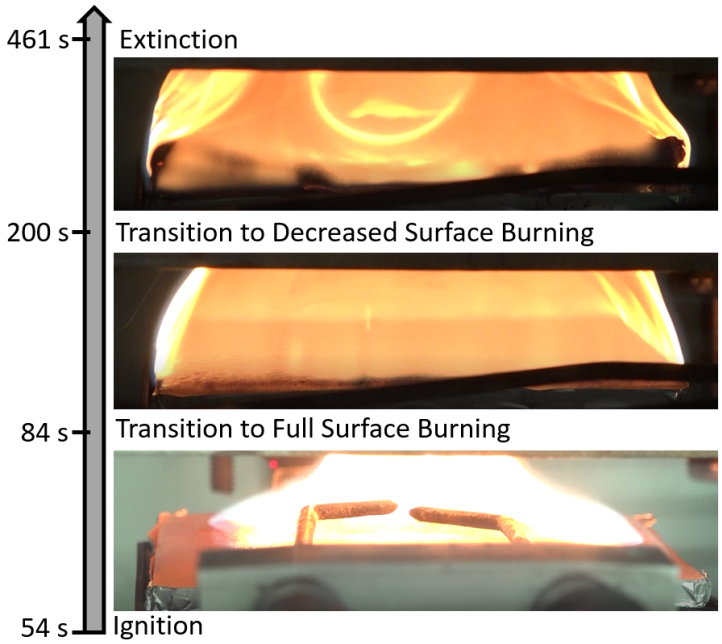

Figure 3.4: Timeline of PBT/GF at 51.5 kW/m^2

Above in figure 3.4, it is seen that instead of material recession, the glasfibers caused the sample to curve up at the edges. This then caused the flame shape to change from the standard pyramid to a horseshoe shape. A similar pattern is obsvered for PBT/GF/Exolit which can be seen in the Appendix. Due to the presence of glasfibers, the decreased surface burning cannot be determined based on material recession; instead, the decreased surface burning point for PBT/GF and PBT/GF/Exolit is considered to be when the burning shape transitions to a horseshoe shape.

3.1.3 Comparison with Other Studies

One way to compare cone calorimeter results among tests is by looking at the reported heats of combustion. The heats of combustion for this project are recorded

in tables 3.2 and 3.3. The initial mass heats of combustion from this project, instantaneous heats of combustion from Leventon et al., and average effective heat of combustion from Quintiere's Fundamentals of Fire Phenomenon are shown below in table 3.4.

Table 3.4: Comparisons of ΔH_c [kJ/g] Between Current Study & Literature

Material	Current Study	Leventon et al. [4]	Quintere [23]
POM	15.3 ±0.35	14.9 ±0.20	13.4
PMMA	25.5 ±0.28	23.8 ±0.20	24.2
HIPS	30.1 ±0.53	27.9 ±0.70	—

The ΔH_c results for Leventon et al. are all slightly lower than the ΔH_c found in this project. This discrepancy could be due to the method of calculating ΔH_c. In this project, ΔH_c was calculated using the initial mass, while Leventon et al. calculated ΔH_c using the average of a quasi-steady portion of the instantaneous ΔH_c vs. time curve. This variation in calculation methods could be the cause of the slightly lower ΔH_c values reported in Leventon et al. [4]. Quintiere reports lower values for heat of combustion of POM and PMMA as well, which could also be due to a different calculation method. While all materials reported in table 3.4 have the same chemical composition, the materials tested by Quintiere could be from different manufacturers which could cause variaton in results. For the most part, ΔH_c values from this project align well with values from the literature.

3.2 Double Heat Flux Gauge Measurements

3.2.1 Raw Data Analysis

Heat flux graphs for the center and side gauges were made for each material at each radiant heat flux prescribed. An example of the untouched raw data for the side heat flux of POM at 20.6 kW/m^2 is shown below in figure 3.5. The raw heat flux data was then adjusted as described below.

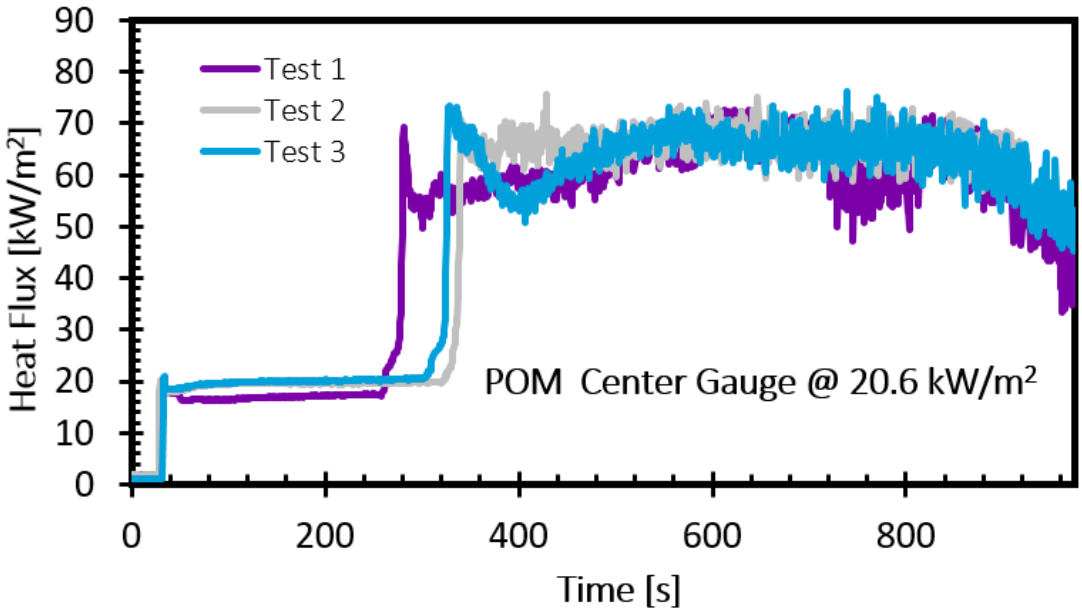

Figure 3.5: Raw data graph for side heat flux of POM at 20.6 kW/m^2

Ignition time is defined when a stable diffusion flame is sustained and there is no more flashing. For all of the materials, ignition time was determined using visual analysis of recorded data and videos. It was then confirmed by observing spikes in a time derivative of the heat flux measurements. As seen in figure 3.5 above, the ignition times are not consistent among tests for the side heat flux of POM at

20.6 kW/m^2. While there is a smaller difference in ignition times for tests at 51.5 kW/m^2, the inconsistency in ignition times is seen for all materials in both the side and center.

The reason that the ignition time for the double heat flux gauge test is not repeatable is due to pre-heating from the cone calorimeter. For the double heat flux gauge tests, the samples were sitting under the cone calorimeter for much longer periods of time than for the standard cone calorimeter tests. A layer of kaowool PM was attached to the bottom of the cone shutter in order to combat this problem; however, clearly some heat was able to escape. Due to this pre-heating, the ignition times for the double heat flux gauge tests are not reliable and only the cone calorimeter ignition times reported in table 3.1 should be considered. In order to make the tests more comparable, the double heat flux gauge ignition time for each test is extracted and set as the starting time for each of the heat flux graphs.

After decreased surface burning occurred, the heat flux gauge readings were no longer reliable. Once the materials receded 3 mm, the gauges were too far from the surface of the material to allow accurate reading of the surface heat flux. Similarly, the heat flux gauge readings are not reliable when the burning pattern changes to a horseshoe shape because the flame shape has a large effect on the heat flux readings; therefore, the heat flux graphs needed to be cut-off at these points. The cutoff points of the graphs were chosen based on the HRR decreased surface burning criteria for the materials with standard flame shapes including POM, PMMA, and HIPS. For PBT/GF and PBT/GF/Exolit the cutoff points on the were chosen solely based on visual observation of horseshoe shape formation.

Heat flux baselines were defined as the contribution of the cone heater to the measured heat flux. In order to isolate the surface heat flux, heat flux baselines measured 30 s prior to ignition were removed. The baselines was determined by taking an average of the heat flux measurements for 30 s before the ignition time. The average heat flux baselines were then subtracted from the raw heat flux data.

An average of the heat flux baselines was taken for each material at each heat flux for the side and center gauges. A ratio of the average side to center heat flux baseline was then calculated for each set. The side/center baseline ratio represents the uneven heating supplied by the cone calorimeter. This gives even more importance to removing the baselines in order to get accurate flame heat feedback data. These values are shown below in table 3.5 with an average of the side/center baseline ratios at the bottom of the table.

Table 3.5: Heat Flux Baseline Ratios

Material	External Heat Flux [kW/m^2]	Side Baseline [kW/m^2]	Center Baseline [kW/m^2]	Side/Center Ratio
POM	20.6	20.1	22.2	0.91
	51.5	51.0	51.2	1.0
PMMA	20.6	20.8	23.9	0.87
	51.5	46.7	52.9	0.88
HIPS	20.6	22.1	22.1	1.0
	51.5	52.5	53.8	0.98
PBT/GF	51.5	53.2	55.0	0.97
PBT/GF/Exolit	51.5	54.7	53.9	1.0
Average				**0.95**

The variations between the side/center baseline ratios are caused by a combination of factors. Throughout the course of experiments, the heater on the cone calorimeter was replaced, which may have an effect on the heating. In addition, in order to prevent arching with the spark igniter, the sample was shifted slightly for each experiment. These factors contribute to the slight variations in baseline ratios between experiments.

A 2008 study by Janssens et al. tested the heat flux distributions on 15 cm square non-flaming samples under the cone calorimeter exposed to various radiant heat fluxes. A heat flux meter was used to measure heat flux through 25 holes that

were drilled through the sample. It was found that heat flux was not homogeneous throughout the area of the sample. This represents that the cone heater is not exactly uniform [24]. These findings support the variations in side and center baselines found in the present study.

3.2.2 Ignition Delay for Flame Spread

The uneven heating of the cone calorimeter causes causes the center of the material to experience higher heat fluxes, which enables the center to ignite first, and then spread to the side. From the double heat flux gauge experiments, it was observed that there was a delay in ignition time from the center to the side for all materials. Table 3.6 shows the average difference in ignition, Δt_{ign}, times from the side to the center. POM has a huge disparity in ignition times. Because there were issues with keeping the POM flat under the cone the ignition times might have been affected; therefore, the POM it will be excluded from the average Δt_{ign}. There is no clear disparity between Δt_{ign} among the different heat fluxes so an average is taken of all the values for PMMA, HIPS, PBT/GF, and PBT/GF/Exolit. The average is found to be 2.53 s.

Table 3.6: Difference in Ignition Times

Material	External Heat Flux [kW/m^2]	Average Δt_{ign} [s] between side and center
POM	20.6	14.63
	51.5	5.17
PMMA	20.6	7.50
	51.5	0.83
HIPS	20.6	0.83
	51.5	3.50
PBT/GF	51.5	1.50
PBT/GF/Exolit	51.5	1.00
Average excluding POM		**2.53**

3.2.3 Establishing the Regions of Steady Heat Flux

After examining the raw data, it is clear that there is a region where the heat flux is steady for most of the materials. The places where unsteady behavior is observed comes from incomplete surface burning before the flames spread to the full surface, and/or issues with gauge readings. The regions of steady heat flux begin when full surface burning is established. All of those times are displayed on the picture

timelines. The ends of the regions of steady heat flux are chosen based on visual criteria from the videos as well as indications of gauge disruptions of decreased surface burning.

An example of the adjusted heat flux data can be seen in figures 3.6 and 3.7. These graphs display the adjusted side and center heat flux data for POM at 20.6 kW/m^2 from ignition time to the cutoff points. Between those points, a region of steady heat flux was chosen which is denoted by the spaces between the vertical dashed lines.

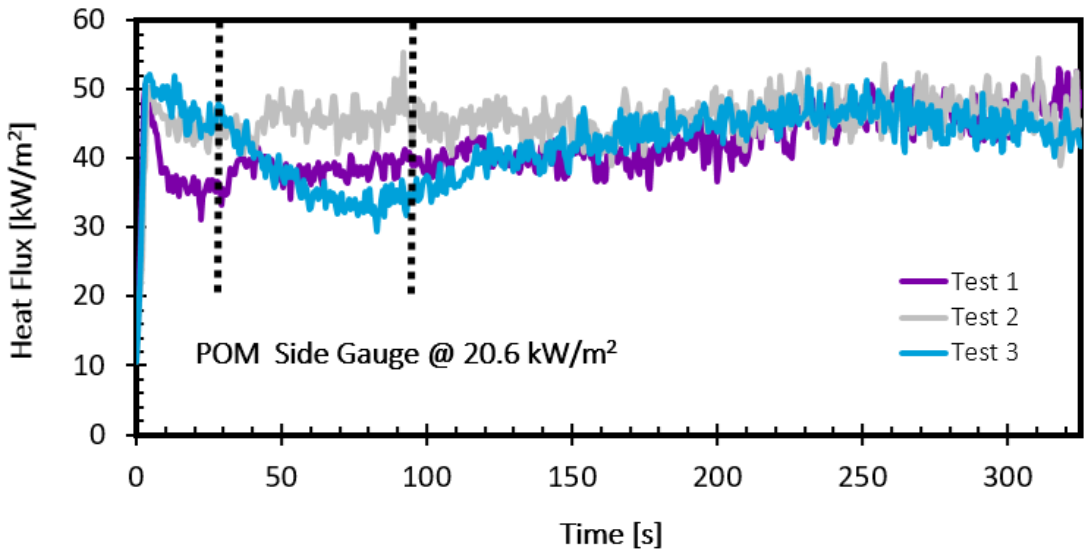

Figure 3.6: Side Heat Flux of POM at 20.6 kW/m^2

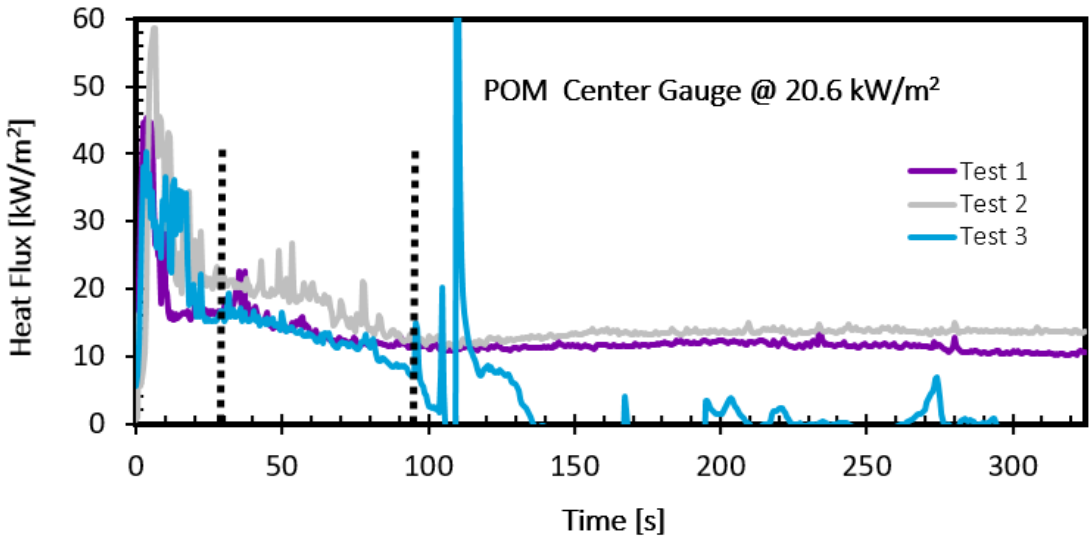

Figure 3.7: Center Heat Flux of POM at 20.6 kW/m^2

Full surface burning for POM at 20.6 kW/m^2 began 28 s after ignition which can be seen in figure 3.3. The end of the region of steady heat flux for POM at 20.6 kW/m^2 was established from the heat flux behavior shown in the graphs. At 95 s, the stability of test 3 of center gauge in figure 3.7 deteriorated and the heat flux of all three tests dropped. This change is likely due to the formation of deposits on the gauge. Gauge deposits can not easily be seen from visual inspection, but are evident from inspection of the gauge surface after each test. For this reason, it is important to inspect every graph for indications of gauge disruptions. This method for ending the region of steady heat flux before gauge disruption was also used for PMMA at 51.5 kW/m^2, HIPS at 20.6 kW/m^2, and PBT/GF/Exolit at 51.5 kW/m^2 which can be seen in the Appendix.

In cases where the decreased surface burning occurred after the graph cutoff points of 50% of the HRR area, and there were no indication of deposits on the

gauges, the region of steady heat flux spans from the full surface burning point until the cutoff point of the graph. This is the case for POM at 51.5 kW/m^2, and PMMA at 20.6 kW/m^2 which can be seen in the Appendix.

3.2.4 Covered Gauge Experiments

Covered gauge tests were performed for PMMA and HIPS at 20.6 kW/m^2 in order to see if soot deposits had an effect on gauge readings. These tests were performed at the lower heat fluxes so that there was enough time to remove the gauges properly. The covered gauge tests were not performed for POM because POM produces minimal soot. They were also not performed on PBT/GF and PBT/GF/Exolit due to limited number of samples. The side and center heat flux graphs for PMMA and HIPS at 20.6 kW/m^2 can be seen below in figures 3.8, 3.9, 3.10, and 3.11 respectively.

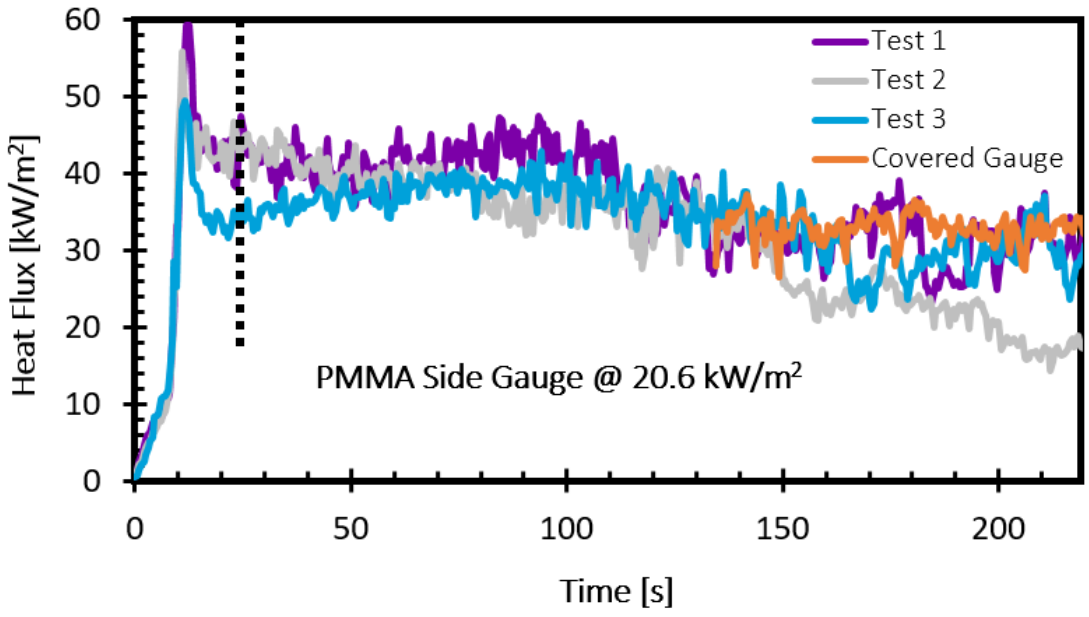

Figure 3.8: Side Heat Flux of PMMA at 20.6 kW/m^2

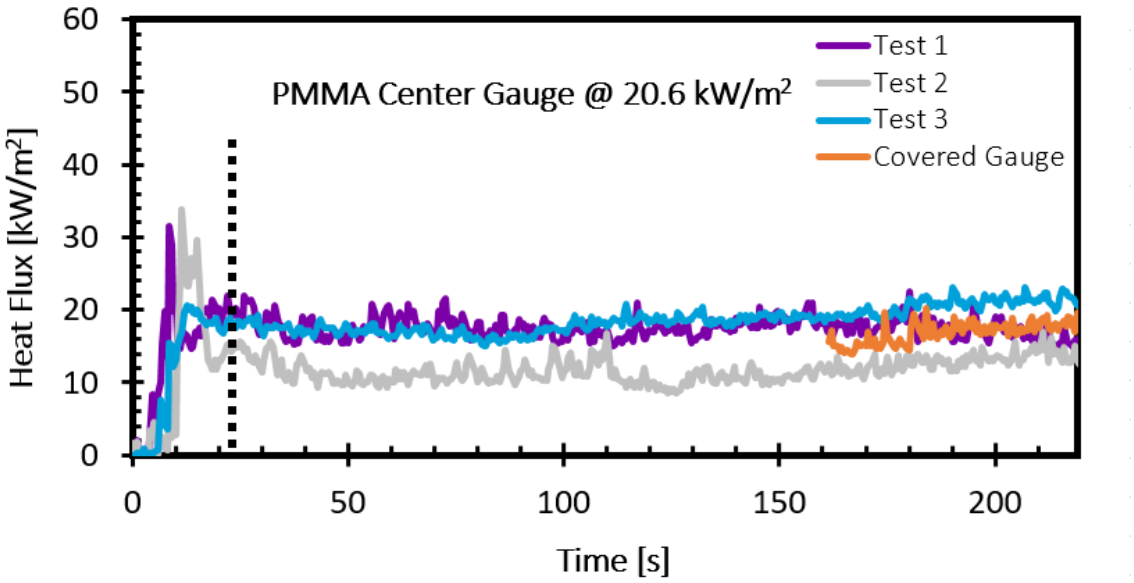

Figure 3.9: Center Heat Flux of PMMA at 20.6 kW/m^2

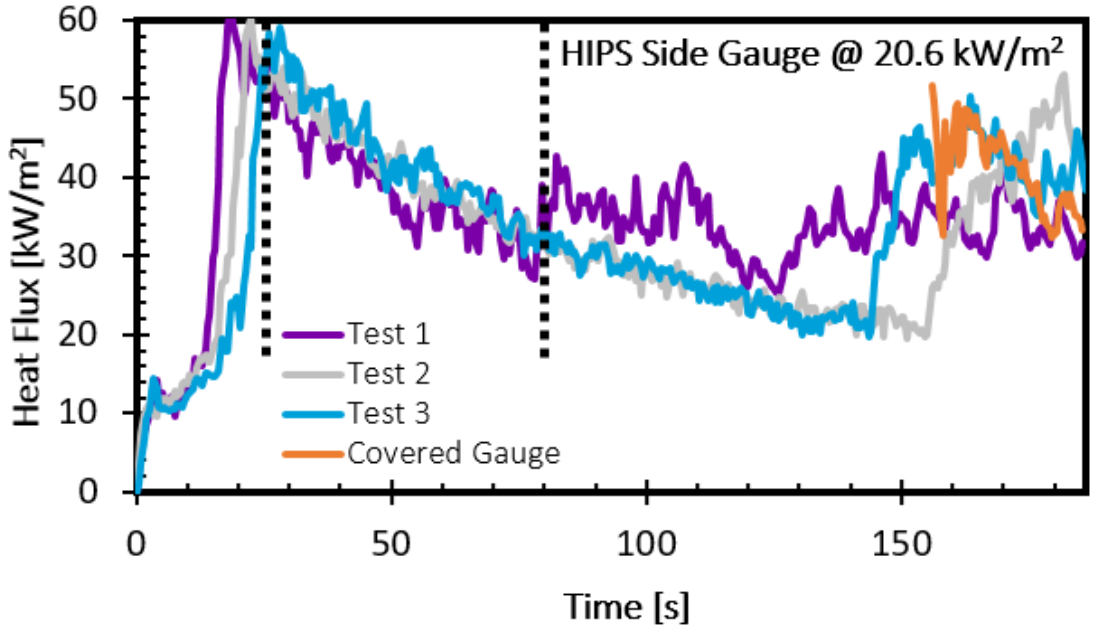

Figure 3.10: Side Heat Flux of HIPS at 20.6 kW/m^2

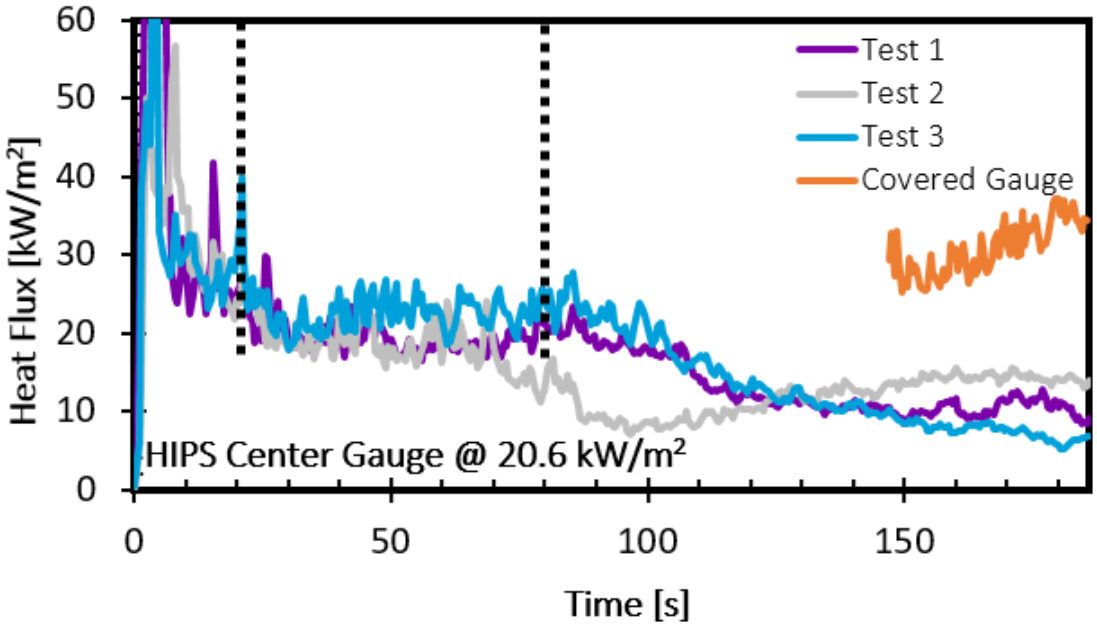

Figure 3.11: Center Heat Flux of HIPS at 20.6 kW/m^2

The covered gauge tests show no difference from the standard tests for PMMA in both the side and the center; therefore, it is clear that the gauge readings are all accurate for the PMMA. The covered test for HIPS is a little high in the center which represents some deposits on the gauge; however, the covered gauge tests are outside of the region of steady heat flux for HIPS at 20.6 kW/m^2. While there may be some soot deposits on the gauges for HIPS at 20.6 kW/m^2, that unreliable portion of the data is not included in the rest of the analysis.

3.2.5 Extended Edge Experiments

The extended edges test was conducted for PMMA at 51.5 kW/m^2 in order to examine edge effects. It was performed on PMMA at 51.5 kW/m^2 because PMMA has relatively uniform behavior at a high heat flux. The side and center heat flux graphs

for PMMA 51.5 kW/m^2 can be seen below in figures 3.12, and 3.13 respectively.

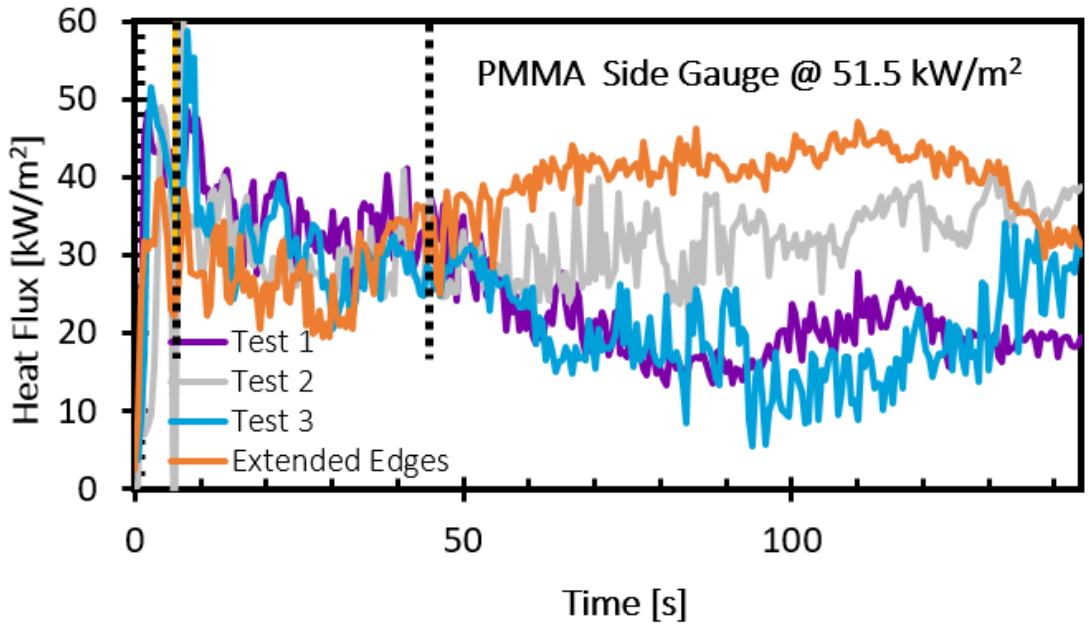

Figure 3.12: Side Heat Flux of PMMA at 51.5 kW/m^2

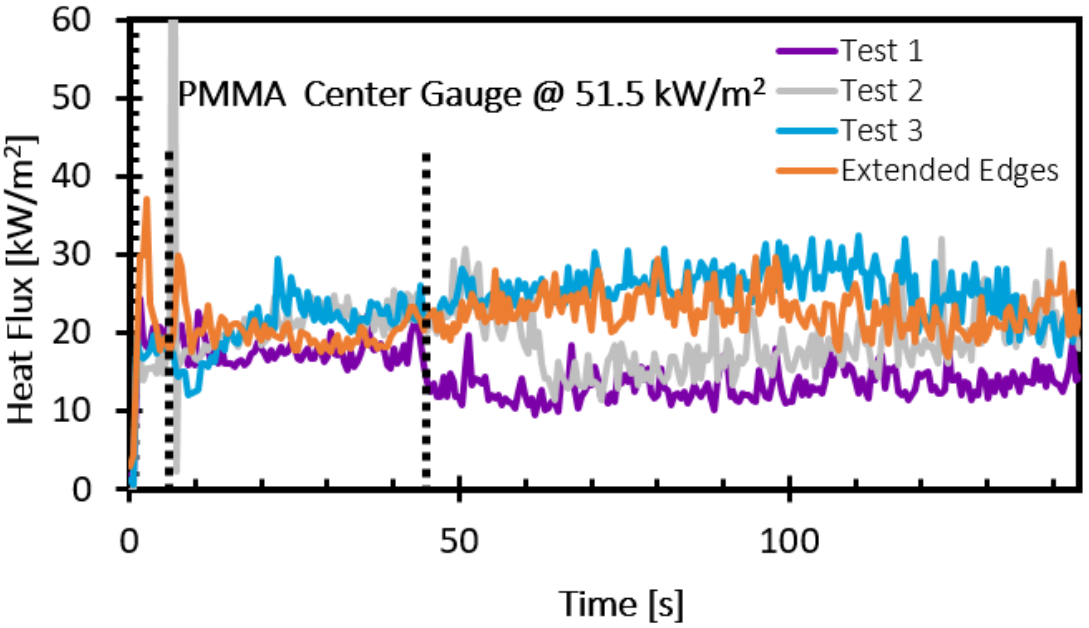

Figure 3.13: Center Heat Flux of PMMA at 51.5 kW/m^2

While the heat flux for the increase edges test for the side gauge is slightly

lower than the standard tests, the difference is small. This test does not indicate significant edge effects.

3.2.6 Experiments Excluded from Further Analysis

Regions of steady heat flux were not able to be selected for HIPS and PBT/GF at 51.5 kW/m^2. The picture timelines and side and center heat flux graphs for HIPS at 51.5 kW/m^2 can be seen below in figures 3.14, 3.15, and 3.16 respectively.

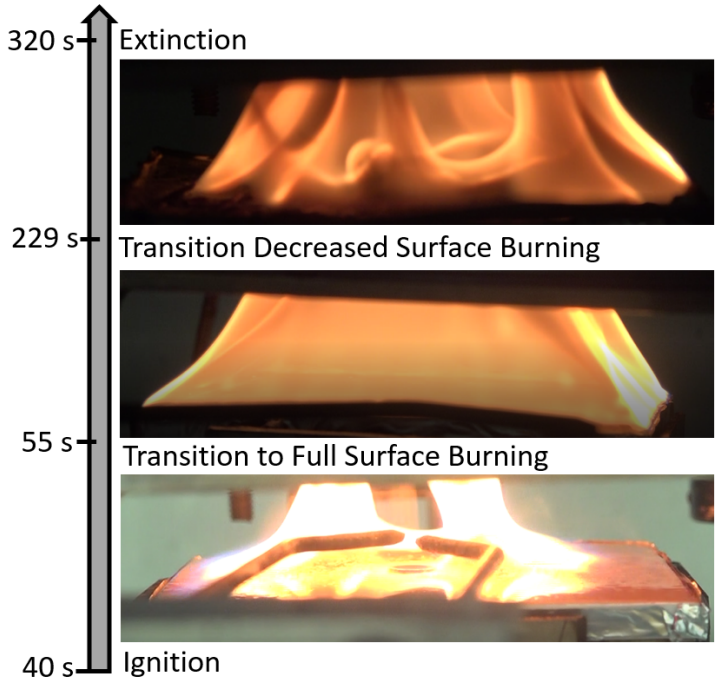

Figure 3.14: Timeline of HIPS at 51.5 kW/m^2

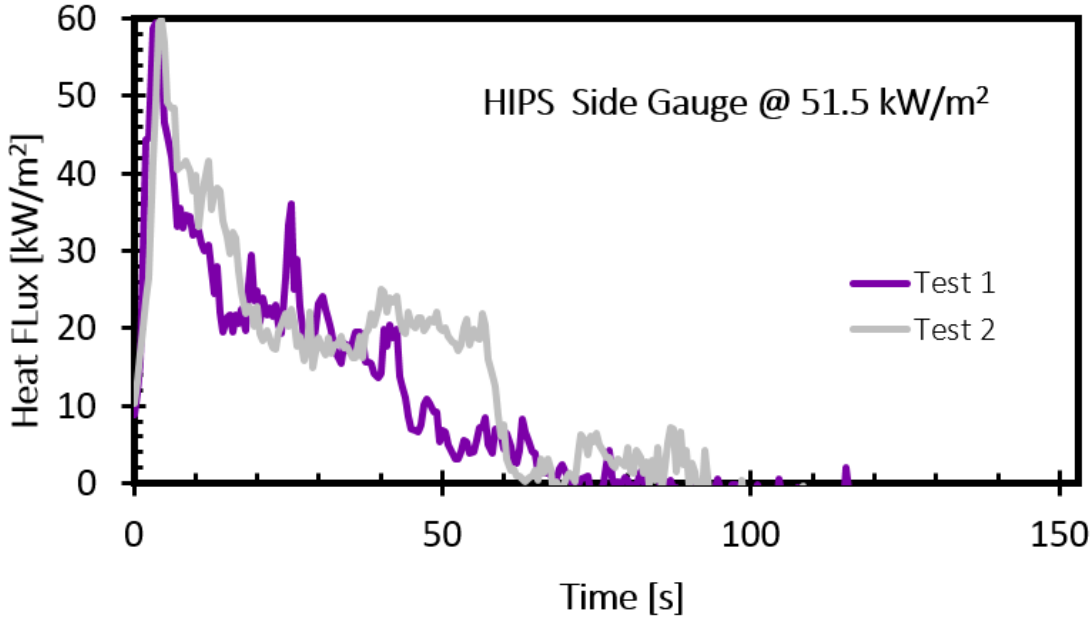

Figure 3.15: Side Heat Flux of HIPS at 51.5 kW/m^2

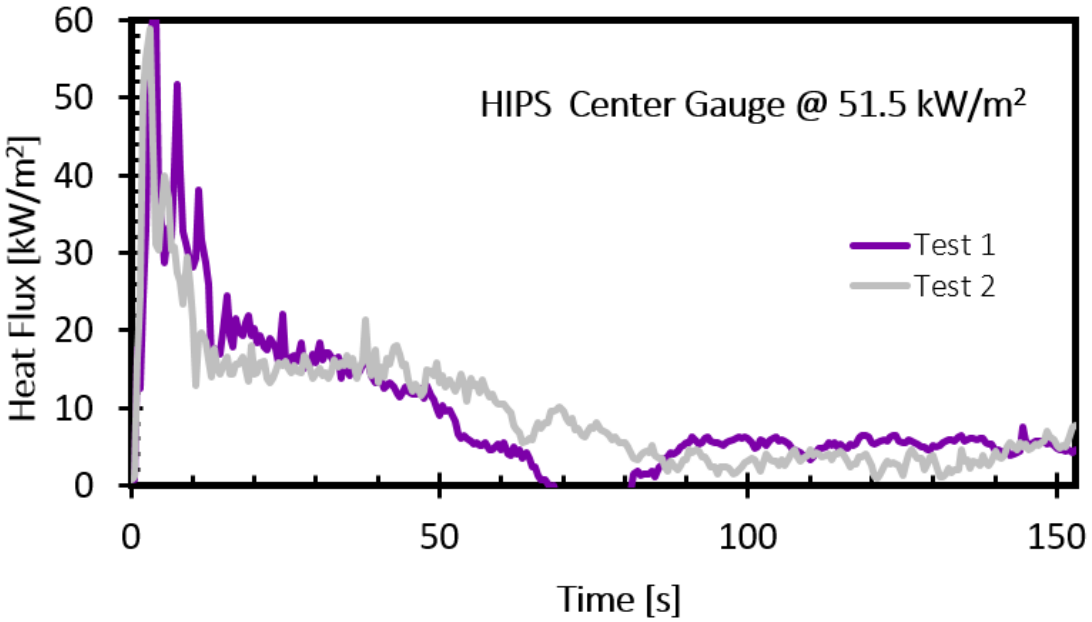

Figure 3.16: Center Heat Flux of HIPS at 51.5 kW/m^2

While the heat flux graphs for HIPS and PBT/GF at 51.5 kW/m^2 show relatively good repeatability between experiments, the heat flux results are extremely

low and unstable for the side gauge. HIPS and PBT/GF are highly sooting materials. This behavior can be seen in the picture timeline in figures 3.14 and 3.4, represented by the dark orange color of the flames. Because the combustion of HIPS and PBT/GF produces so much soot, a significant portion of heat from the heater is absorbed by the flame, which can cause inaccurate and low heat flux data. The percentage of heat absorption is also increased for the materials tested at higher external heat fluxes. This is one reason why the heat flux is so low for the side gauge measurements.

Figure 3.17: PBT/GF Sample After Completion of Double Heat Flux Gauge Experiment

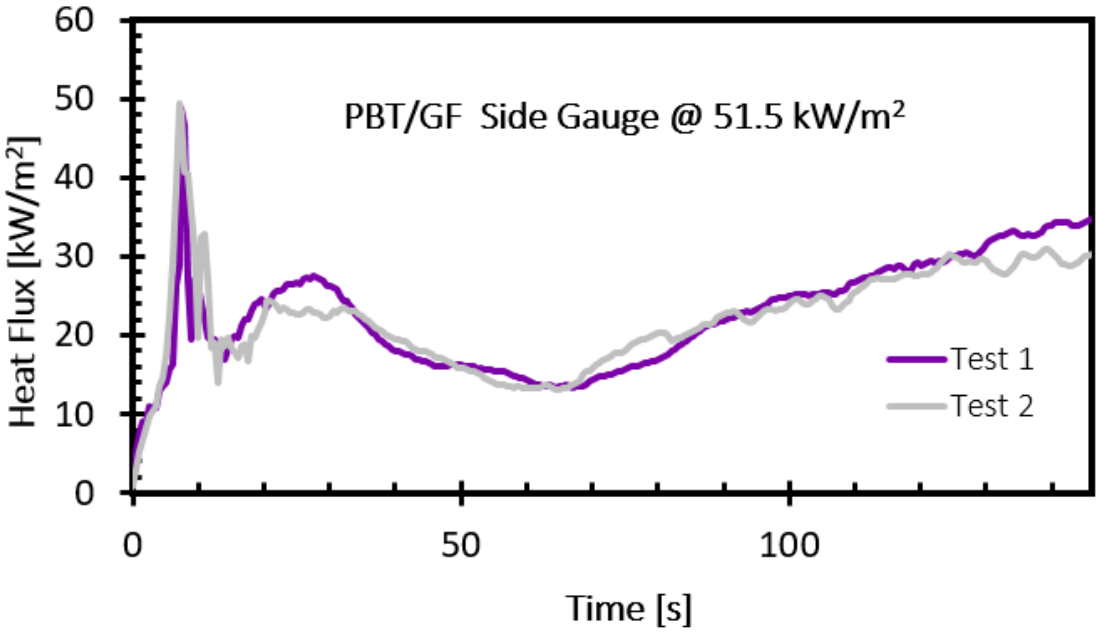

Figure 3.18: Side Heat Flux of PBT/GF at 51.5 kW/m^2

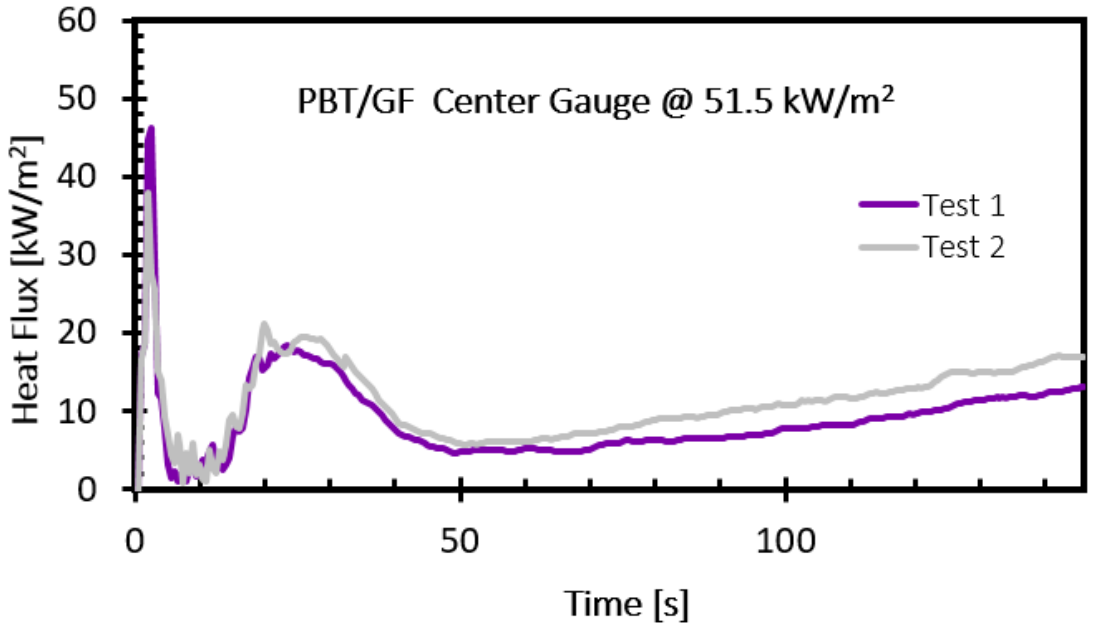

Figure 3.19: Center Heat Flux of PBT/GF at 51.5 kW/m^2

Although soot deposits on gauges could not be observed during experiments, insulating bubbles were sometimes seen on the gauges after the experiments were

completed. This was the case for the PBT/GF experiments. A picture of the PBT/GF post-experiment can be seen in figure 3.17 with insulating bubbles covering the holes where the gauges were during the experiments. The side and center heat flux graphs for PBT/GF at 51.5 kW/m^2 can be seen in figures 3.18, and 3.19 respectively. These bubbles cover the gauges and prevent them from getting accurate heat flux measurements.

3.2.7 Average Heat Fluxes

The heat fluxes (HF) within the selected regions of steady heat flux for each experiment were time averaged across tests to obtain a representative value. These HF values for side and center gauges can be seen in figures 3.20 and 3.21 respectively. The standard error for these values was also calculated and is represented by the error bars on the graphs.

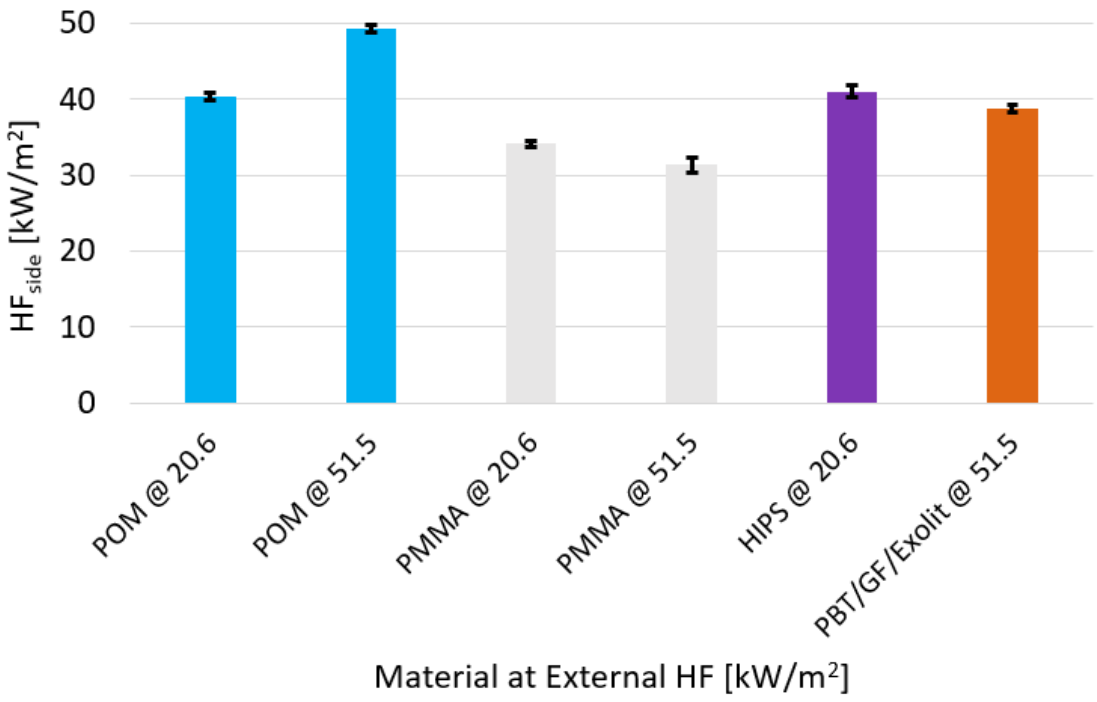

Figure 3.20: Average Measured Heat Flux from the Side Gauges for each Material

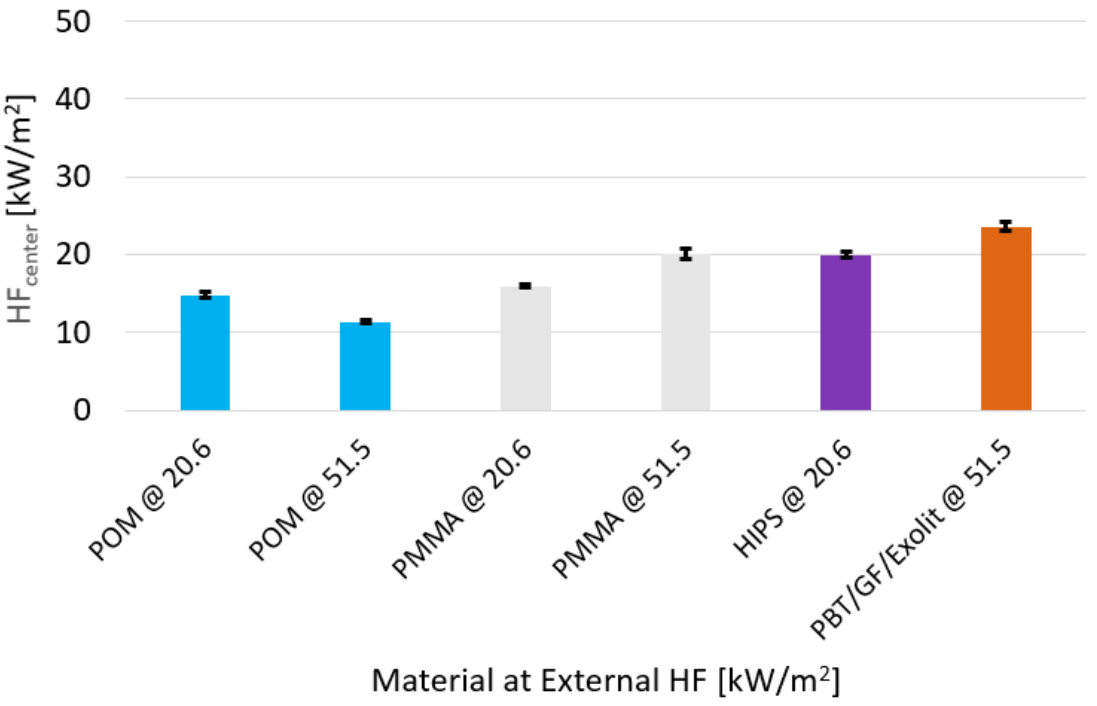

Figure 3.21: Average Measured Heat Flux from the Center Gauges for each Material

In order to provide an option for further comparison, the average heat fluxes provided in figures 3.20 and 3.21 are combined between the low and high external heat fluxes. These combined heat fluxes are shown with the standard error below in table 3.7.

Table 3.7: Combined Heat Fluxes

Material	Center Heat Flux [kW/m^2]	Side Heat Flux [kW/m^2]
POM	12.2 ±0.17	47.1 ±0.39
PMMA	16.8 ±0.23	33.6 ±0.38
HIPS	20.0 ±0.33	41.0 ±0.75
PBT/GF/Exolit	23.6 ±0.57	38.7 ±0.50

3.2.8 Comparison with Other Studies

In 1996, Rhodes and Quintiere used a heat transfer analysis to find that heat flux for black PMMA could be modeled as a constant 37 kW/m^2. Their experimental results with a 10 cm square methane burner showed that the total flame heat flux was a constant 27 kW/m^2 [15]. In this project, total flame heat flux for PMMA, which is an average of the side and center measured heat flux values for PMMA, is 25 kW/m^2. This is significantly lower than the theoretical value calculated from heat transfer analysis (37 kW/m^2) found in the 1996 study; however, the theoretical model makes many assumptions including assuming constant material properties,

a quadratic temperature profile, and constant net heat flux to the surface to name a few. Due to the assumptions made in the theoretical model, the experimental results in this study are a more accurate representation of heat flux. Rhodes and Quintiere were not able to conduct experiments under the cone calorimeter with accurate heat flux measurements due to material condensation, so they resorted to using a methane burner without a sample to measure heat flux. Those measurements produced a lower heat flux that is closer to the average heat flux found in this study; however, their experimental method is not representative of flame heat flux for select plastics because no monomers were used in the methane burner experiments.

Beaulieu and Dembsey's 2008 results for flame heat flux are shown in table 1.1. The results for total flame heat flux for black PMMA and black POM are 20 and 11 kW/m^2 respectively [1]. Because heat flux was measured in the center of the samples, they should be compared to the average measured value from the center gauges for clear PMMA and white POM from this study which are 12 and 17 kW/m^2 respectively. The values found in this study are very close to those found in the 2008 study, even though the experiments were conducted under different apparatuses. The AFM was used in the 2008 study, with samples that were about 25 mm thick, while 6 mm thick samples were tested under the cone calorimeter for this project. In addition, a much wider range of external heat fluxes were tested with the AFM, while the samples in this project were only exposed to two external heat fluxes under the cone calorimeter. These differences could explain the small variation in results.

In 2009 Stoliarov et al. used inverse modeling to find flame heat flux in a range

of 11 to 24 kW/m^2 for a spectrum of materials. This range was then compared to the average value for black PMMA and black POM, 16 kW/m^2, found in Beaulieu and Dembsey's study. Because the range that Stoliarov et al. found was small, it was determined that the value of 16 kW/m^2, which was within this small range, was an acceptable value for first order approximation of flame heat flux [18]. While the results in this project are comparable to those of Stoliarov et al. and Beaulieu and Dembsey, the cone calorimeter was only used in this project; therefore, the results from this project are the most representative of surface heat flux of materials under the cone calorimeter.

So far, all heat flux results have been compared with the center heat fluxes found in this study. One study that can be used to compare the side heat flux results is the 2107 study from Leventon et al. The 2017 study tested heat flux at the edge of vertical samples of varying heights over time. Because the 2017 study included vertical flame spread, it is important to only compare values once the flames have reached the edges. The plateaus on the graphs from the 2017 studies represent the time at which the flame is at the edge of the sample [4]. The smaller 5 cm samples used in Leventon et al. have minimal flame spread and are closer in geometry to this study, so the average values of the 5 cm plateaus from Leventon et al. were compared with the average side heat flux values from this study as opposed to different heights. Those average values from Leventon et al for POM, PMMA, and HIPS are around 48, 35, and 37 kW/m^2 respectively [4]. As reported in table 3.7, the combined side heat fluxes found in this project for POM, PMMA, and HIPS are 47.1, 33.6, and 41 kW/m^2 respectively. These values are all very close to those

found in Leventon et al.

For both the 2017 study and this project, the side heat flux for POM which is significantly higher than the other materials. The explanation provided by Leventon et al. for this phenomenon is that POM is the least sooting of all the materials used. The soot layer produced from combustion of the other materials absorbs some of the heat energy, causing the surface heat fluxes to appear lower [4]. The findings from this project support that hypothesis.

In 2017, Boyer found heat flux over the whole surface of a sample. Boyer used CFD simulations to determine both radiative and convective heat flux under different external heat fluxes. He found that the center of the sample was ruled by radiation, and the side of the sample was dominated by convection which aligns with the findings in this project [3]. The heat flux findings for 26.5 mm thick samples of PMMA and HIPS with imposed heat fluxes of 25 and 50 kW/m^2 are listed in table 3.8. The average center heat flux values listed in table 3.8 are averages from the radiation-dominated portion of Boyer's findings and the side heat flux values are average peaks from the convection-dominated portion of Boyer's findings. For comparison purposes, the average heat flux values from the present study are also listed in table 3.8.

Table 3.8: Heat Flux Comparison between the Present Study and Boyer's Study [3]

Material	External HF [kW/m^2]	Study	Average Center HF [kW/m^2]	Average Side HF [kW/m^2]
PMMA	low	Boyer	5	11
		present study	16	20
	high	Boyer	5	9
		present study	20	31
HIPS	low	Boyer	5	16
		present study	20	41

Two major differences are that while this project found a small portion of the heat flux in the center to be convective, Boyer finds that the center is almost all radiative [3]. Similarly, while this project finds that the side heat flux is all convection, Boyer finds that the center heat flux is dominated by convection with a small radiative component. In general, the heat fluxes found in Boyer's simulations are about 66% lower than those found in this project; however, the overall trends for convection and radiation along the surface between Boyer's results and this project are very similar.

In 2017, Alibert et al. measured heat flux in the center of a PMMA sample and found that the center was consistently ruled by radiation. Alibert et al. found that the radiative portion of the center heat flux was 65% and the side portion was 35% [22]. In this study, the average total heat flux for PMMA in the center was found to be 16.8 kW/m^2. The convective portion of the heat flux was assumed to

be a constant 6.87 kW/m^2; therefore, the radiative percentage of the heat flux for PMMA in the center found in this study is 59% and the convective percentage is 41%. Although different apparatuses were used in Alibert et al. and the present study, the radiative/convective percentages found were consistent.

Chapter 4: Discussion and Analysis

4.1 Developing the Model

In the present study, only total heat flux has been measured; however, in the literature, there were several studies examining the radiative portion of the heat flux. In order to understand the radiative portion of the heat flux, the combined heat fluxes in table 3.7 are compared to the radiative fractions in table 4.1. It can be seen that center heat fluxes for each material follows the pattern of rising radiative fractions. Because of this pattern, the average heat flux for the center gauges is graphed against χ_r and a line of best fit is overlayed in figure 4.1. The line of best fit for this graph is $HF_{center} = 27.09\chi_r + 6.87$ where HF is the heat flux, 27.09 $kW/m^2\chi_r$ is the radiative portion of the heat flux, and 6.87 kW/m^2 is the convective portion of the heat flux.

Table 4.1: Radiative Fractions [4]

Material	FPA	Cone Calorimeter	Average
POM	0.22	0.22	0.22
PMMA	0.33	0.33	0.33
HIPS	0.50	0.49	0.50

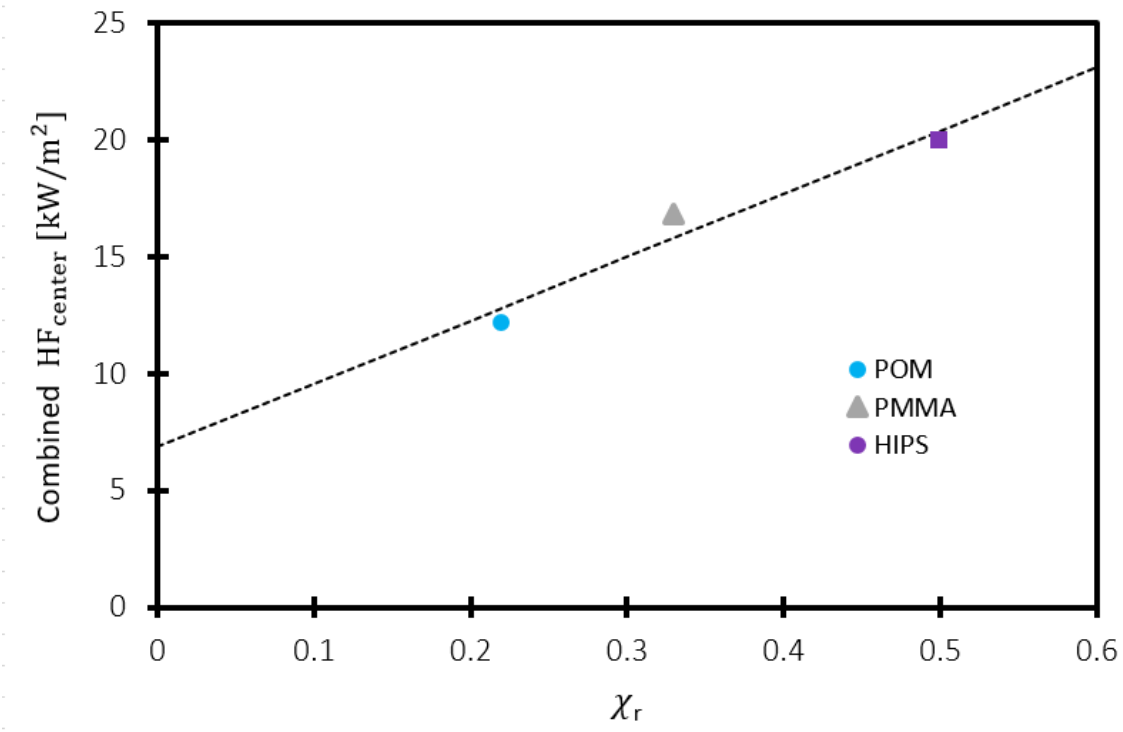

Figure 4.1: Average Measured Center Heat Flux (error bars too small to be displayed on the graph)

Heat transfer coefficients are preferred for use in the models rather than HF. Equation 4.1 below is used to model heat flux for the center gauge where h is the heat transfer coefficient, and T_{gauge} is the average temperature of the water that flows through the gauge which was measured as 291 K. T_{flame} is the average adiabatic

flame temperature among materials, calculated by Leventon et al. based on heat of combustion, shown in table 4.2 as 2154 K.

$$h = \frac{HF_{center}}{(T_{flame} - T_{gauge})} \tag{4.1}$$

Table 4.2: Flame Temperatures [4]

Material	Flame Temperature [K]
ABS	1980
HIPS	1890
PBT	2170
PMMAcast	2320
PMMAext	2280
POM	2290
PP	2160
UP	2140
Average	**2154**

In order to obtain a radiative heat transfer coefficient for the center zone, the radiative portion of the of the heat flux obtained from the line of best fit, $HFC_{center,rad} = 27.09$ kW/m^2 is used in equation 4.1 to represent HF_{center}. For the convective heat transfer coefficient for the center zone, the convective portion of the of the heat flux obtained from the line of best fit, $HF_{center,conv} = 6.87$ kW/m^2 is used in equation 4.1 to represent HF_{center}. The radiative heat transfer coefficient,

$h_{center,rad}$, is found to be 14.54χ_r W/m^{2}K and the convective heat transfer coefficient, $h_{center,conv}$, is found to be 3.69 W/m^{2}K.

Comparing the combined heat fluxes in table 3.7 and the radiative fractions in table 4.1, it can be seen that side heat fluxes do not have a distinct relationship to radiative fractions. This indicated that the side experiences purely convective heating, and HF_{side} has no relationship to χ_r. It can be seen in figure 4.2 that POM has an exceptionally high HF_{side} which has been seen before in the literature; therefore, an average is taken between HF_{side} for PMMA and HIPS which is represented by the dashed line. The average value of the dashed line which represents $HF_{side,conv}$ is 37.30 kW/m^2. It is then calculated that $h_{side,conv}$ is 20.02 W/m^2K.

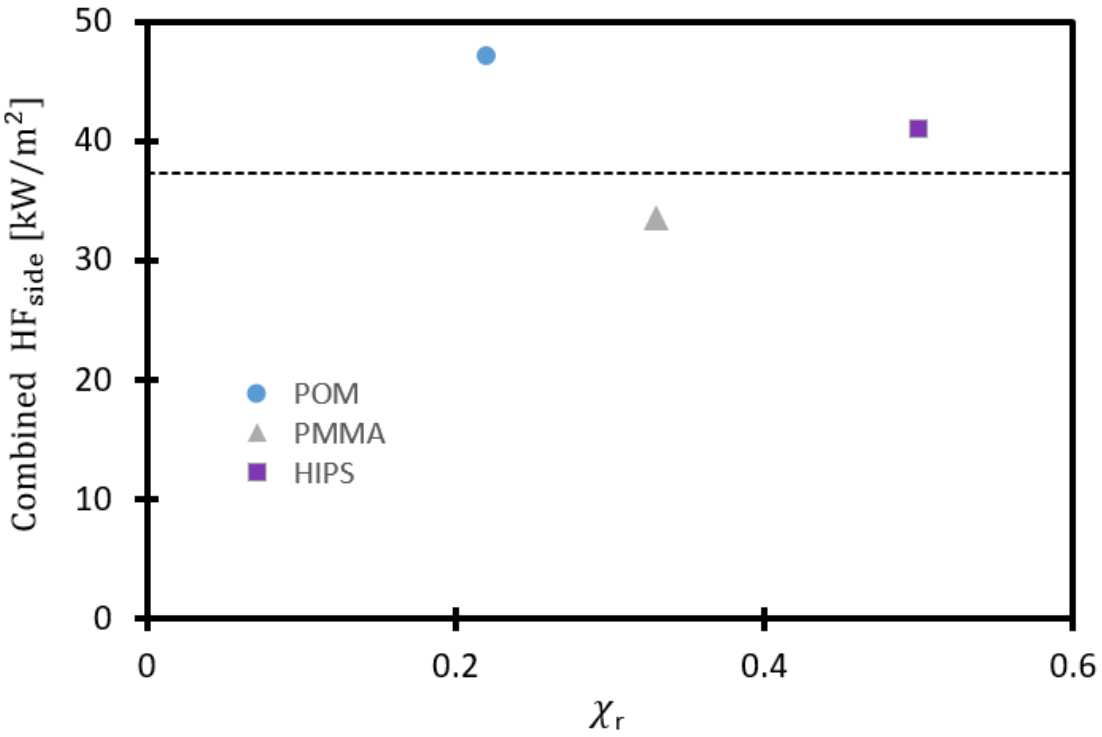

Figure 4.2: Average Measured Side Heat Flux (error bars too small to be displayed on the graph)

4.1.1 Defining the Areas of the Two-Zone Model

The present study has established both radiative and convective heat fluxes and heat transfer coefficients for the side and center. A piece-wise function is desired for use in ThermaKin to simplify the modelling process and conserve computational time; therefore, this analysis will provide two distinct regions one for convection and one for radiation. The areas of the two zones needed to be defined. To determine the portion of the sample area that is governed completely by convection and encompasses the side zone, heat transfer over the surface is considered. The pyrolysing samples are simplified as horizontal hot plates governed by buoyancy-driven free convection. The Rayleigh (Ra) number is calculated with the equation below [5].

$$Ra_L = \frac{g\beta(T_s - T_\infty)L^3}{\nu\alpha} \tag{4.2}$$

The thermophysical properties of air required in this equation are interpolated from the Fundamentals of Heat and Mass Transfer textbook at temperature $\bar{T}$ [5]. $\bar{T}$ is the average between flame temperature (2154 K) and environmental temperature (291K) which is 1222.5 K. The values used are listed below in table 4.3.

Table 4.3: Thermophysical properties for air at 1222.5 K [5]

Property	Symbol	Value
Gravity	g	9.81 m/s^2
Beta	β	0.000818 K^{-1}
Flame Temperature	T_s	2154 K
Environmental Temperature	T_∞	291 K
Kinematic Viscosity	ν	$1.68 \times 10^{-}4$ m^2/s
Thermal Diffusivity	α	$2.31 \times 10^{-}4$ m^2/s
Prandtl number	Pr	0.726

The Ra number is calculated in respect to increasing L, which is the characteristic length. The charecteristic length is calculated from the area divided by the perimeter. This simplifies to r/2, where r is the distance from the edge of the sample to the end of the side zone, or complete convection area. The Ra number is then used in the correlations below for a horizontal heated upward-facing plate to calculate the Nusselt (Nu_L) number in respect to changing Ra number [25].

$$Nu^T = 0.835\bar{C}_l Ra^{1/4} \tag{4.3}$$

$$Nu_l = \frac{1.4}{ln(1 + 1.4/Nu^T)} \tag{4.4}$$

$$Nu_t = C_t^U Ra^{1/3} \tag{4.5}$$

$$\bar{Nu} = (Nu_l^{10} + Nu_t^{10})^{1/10} \tag{4.6}$$

In the equations above, Nu^T represents the laminar thin layer Nu number which is used to calculate which represents the laminar Nu number, Nu_l. Nu_t represents the turbulent Nu number, and $\bar{Nu}$ represents the combined Nu number. The coefficients $\bar{C}_l$ and C_t^U used in the Nu number calculations are found using relationships with the Prandtl number (Pr) in the equations below [25].

$$\bar{C}_l = \frac{0.671}{[1 + (0.492/Pr)^{9/16}]^{4/9}} = 0.516 \tag{4.7}$$

$$C_t^U = 0.14(\frac{1 + 0.0107Pr}{1 + 0.01Pr}) = 0.140 \tag{4.8}$$

The $\bar{Nu}$ number is also equal to the equation below where $\bar{h}$ is the spatially-averaged convective heat transfer coefficient, L is the characteristic length, and k is the thermal conductivity. The thermal conductivity is interpolated at an air temperature of 1427 K, which is the average of the flame temperature and the solid temperature (700K) [5].

$$\bar{Nu}_L = \frac{\bar{h}L}{k} \tag{4.9}$$

Once $\bar{h}$ was found using the equation above, the equations below are used to differentiate $\bar{h}$ with respect to L, to find the local convective heat transfer coefficient, h.

$$h = \frac{d}{dL}(L\bar{h}) \tag{4.10}$$

A second-order, central differential scheme is used to compute the derivative of $\bar{h}$. h is then graphed against r, which is the distance from the edge of the sample and is equal to double the characteristic length L in figure 4.3. The convective heat transfer coefficients for the center and side are overlaid on this correlation graph in order to determine how the results of this project relate to the heat transfer model. Compared to the model from the literature, the heat transfer coefficients found in this project follow a slightly greater slope, but generally show reasonably good agreement.

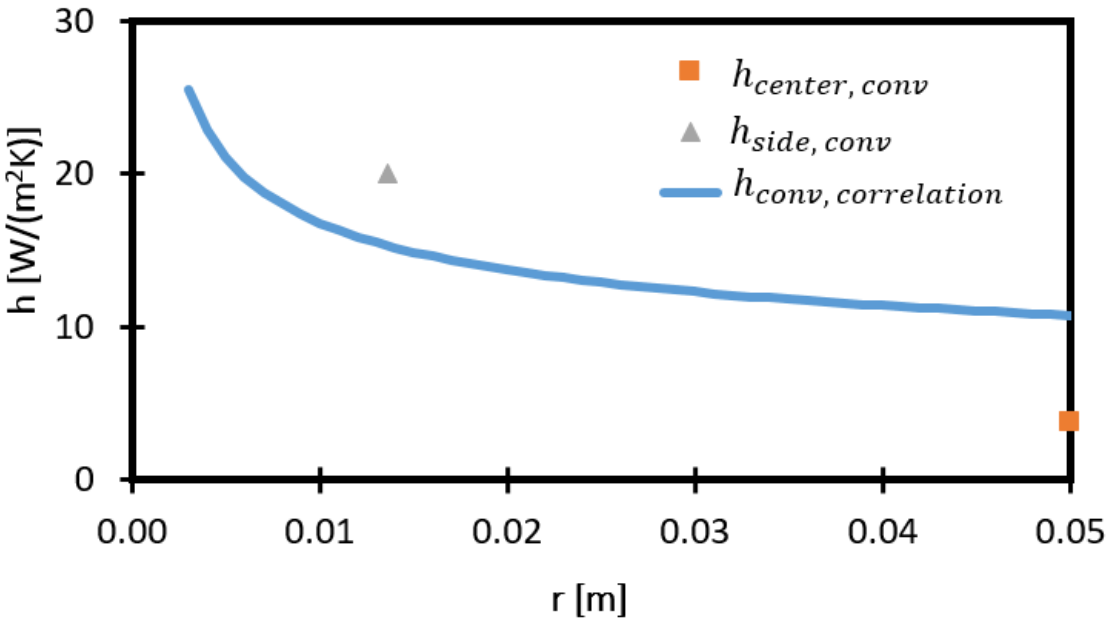

Figure 4.3: Local Convective Heat Transfer Coefficient vs. the Distance from the Sample Edge

From figures 4.1 and 4.2, it was observed that the center heat flux is dominated

by radiation, while the side is dominated by convection. The convective portion of the heat flux decreases with increasing distance from the edge, assuming a constant temperature difference. The critical threshold of the convection-dominated area was chosen as when the convective heat flux is twice as high as the radiative heat flux. In order to determine the distance from the edge of the sample to the end of the convection-ruled area, heat flux vs. r is examined, which can be seen in figure 4.4.

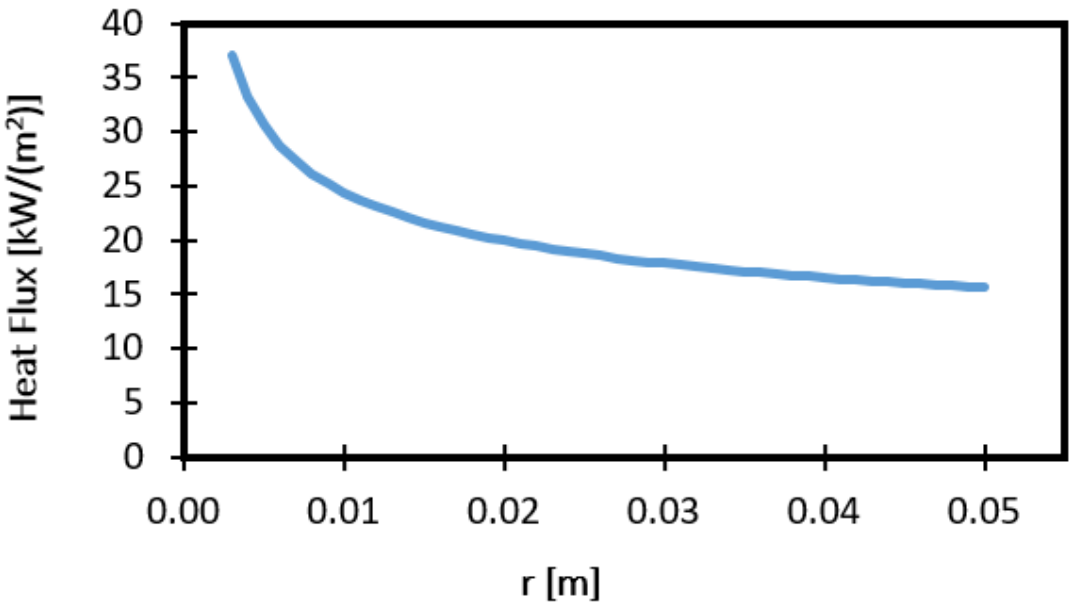

Figure 4.4: Heat Flux vs. the Distance from the Sample Edge

Using figure 4.1, the radiative heat flux is found by subtracting the convective portion ($HF_{center,conv}$ = 6.87 kW/m^2) from the total heat flux in the center when χ_r=0.35 (HF=16.35 kW/m^2) to get 9.48 kW/m^2, which is representative of all the thermoplastics in this project. The convective portion of the heat flux is twice as high as the radiative portion when the convective portion is 18.96 kW/m^2. This corresponds to an r of 0.024 m. This convective distance is shown on the sample in figure 4.5.

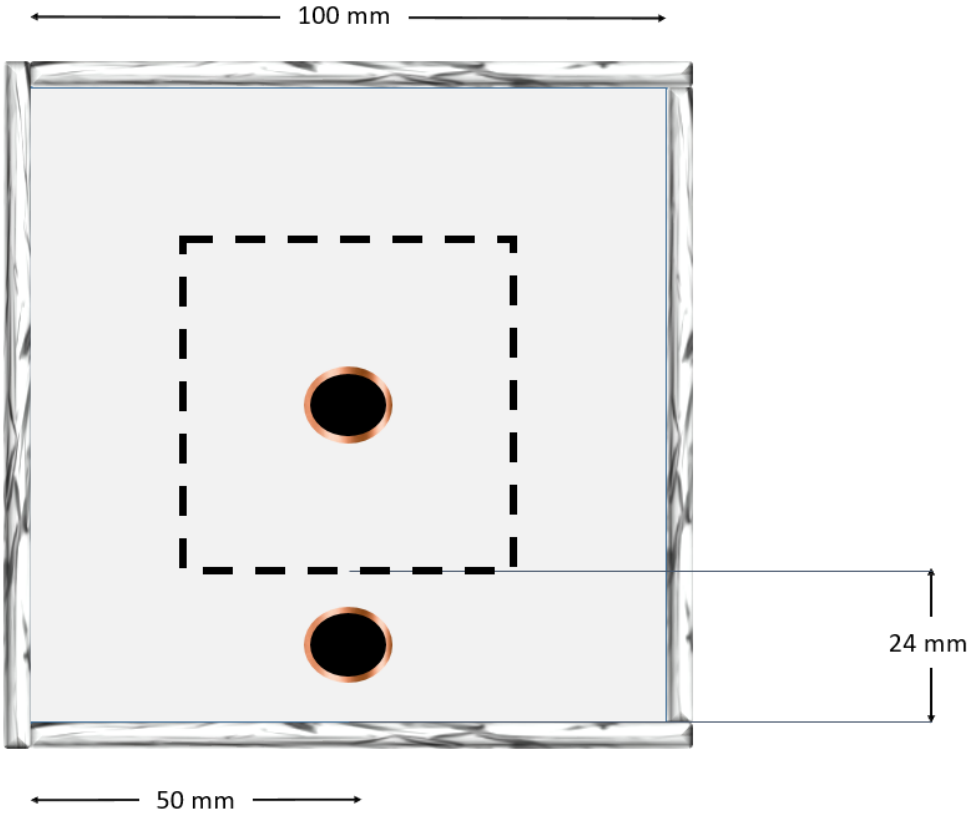

Figure 4.5: Two-Zone Areas Divided by Dashed Line

4.1.2 Comparison with Other Studies

While Boyer did not define a complete convection area, he found that on average the area dominated by convection encompasses 10 - 15 mm from the edge [3]. This is about half the distance found in this project which was 24 mm. While most of Boyer's results are about half of the values found in this project, the convective and radiative heat flux results match the pattern found in this project.

4.2 Summary of the Model

A summary of the inputs for the model is listed below in table 4.4. This summary includes side and center heat flux and heat transfer coefficients, complete convection area, and ignition delay times between the center and side. The relationship between the center convective and radiative heat flux and heat flux coefficients is shown below.

$$HF_{center} = HF_{center,conv} + HF_{center,rad}\ \chi_r \tag{4.11}$$

Table 4.4: Summary of Model

Model Input	Symbol	Value
Heat Flux Coefficient	$HFC_{center,rad}$	27.1 kW/m^2
Heat Flux	$HF_{center,conv}$	6.9 kW/m^2
	$HF_{side,conv}$	37.3 kW/m^2
Heat Transfer Coefficient	$h_{center,rad}$	$14.5\chi_r$ W/m^2K
	$h_{center,conv}$	3.7 W/m^2K
	$h_{side,conv}$	20.0 W/m^2K
Complete Convection Distance from the Edge	r	0.024 m
Ignition Delay Time from Center to Side	$t_{ign,delay}$	2.5 s

Chapter 5: Conclusions and Future Work

5.1 Conclusions

The cone calorimeter is used regularly to test materials and ascertain their HRR, MLR, as well as material properties. In the past ten years, there has been a large effort to develop pyrolysis models, like ThermaKin, that can predict the HRR, and MLR of materials in bench scale apparatuses like the cone calorimeter. These models can greatly reduce the cost and time spent to understand material burning that comes with iterative testing. An important input into these models is the flame heat feedback. Characterizing the flame heat feedback for different materials helps to develop their flame spread models.

There have been a few attempts at characterizing flame heat feedback for vertical flame spread models; however, until recently, there had been no comprehensive studies to develop detailed heat feedback models for horizontal geometry under the cone calorimeter exposed to an external heat flux.

The goal of this project was to develop a new and improved flame heat feedback model to represent cone calorimeter experiments. Several thermoplastics were tested under the cone calorimeter under low and high external heat fluxes. Both standard cone calorimeter experiments and double heat flux gauge experiments were

performed under the cone calorimeter. The double heat flux gauge experiments included one water-cooled heat flux gauge threaded through the center of the 10 cm square samples and one gauge threaded through the side of the sample. HRR and MLR data was collected from the standard cone calorimeter experiments and heat flux data was collected from the double heat flux gauge experiments.

The heat flux gauge data was analyzed thoroughly. Regions of steady heat flux were found that represent the clear gauge readings. Those regions were averaged and used to find radiative and convective heat transfer coefficients for the model. After analyzing the heat flux results, it was determined that the side heat flux is ruled completely by convection while the center experiences convection and radiation, but is dominated by radiation.

A heat transfer analysis was used to define the convection and radiation dominated areas of the two-zone model. The convection-dominated area was defined as the region where the convective heat flux was at least twice as high as radiative heat flux. From that characteristic, a step function was developed to model side and center heat feedback.

While there are no other models that measured horizontal heat feedback for thermoplastics to the extent of this project, the heat flux data found shows relatively good agreement with prior measurements in other studies. When this model is combined with ThermaKin, it should improve ThermaKin's predictive capabilities for horizontal material burning.

5.2 Future Work

In the future, this model will be incorporated into ThermaKin simulations. The results of these simulations will be compared with the experimental measurements of HRR and MLR for horizontal cone calorimeter experiments. In order to make a more robust model, more materials should be tested in a similar fashion - reaching past the scope of thermoplastics. The combustion of different classifications of materials can produce different flame patterns and different heat feedback; therefore, distinctive heat feedback models should be developed based on material classification. More heat flux gauge locations should also be tested in order to verify the total convection area, instead of relying on theoretical analysis. Additionally, in order to understand edge effects better, larger samples could be tested under a bigger cone calorimeter.

Chapter A: Appendix

A.1 Heat Release Rate and Mass Loss Rate Graphs

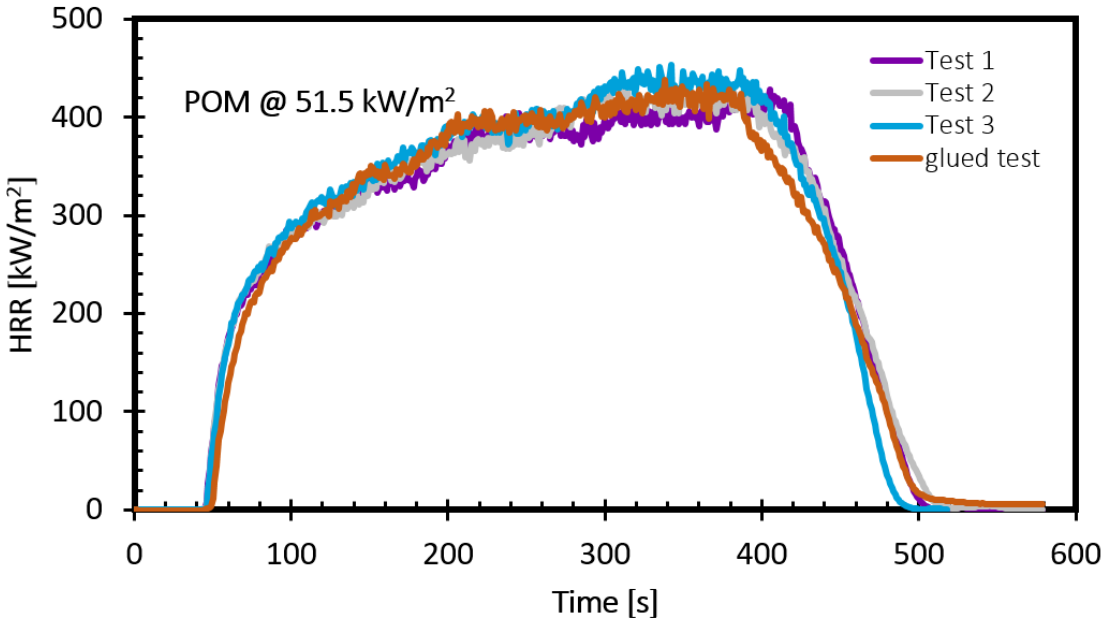

Figure A.1: Heat Release Rate for POM at 51.5 kW/m^2

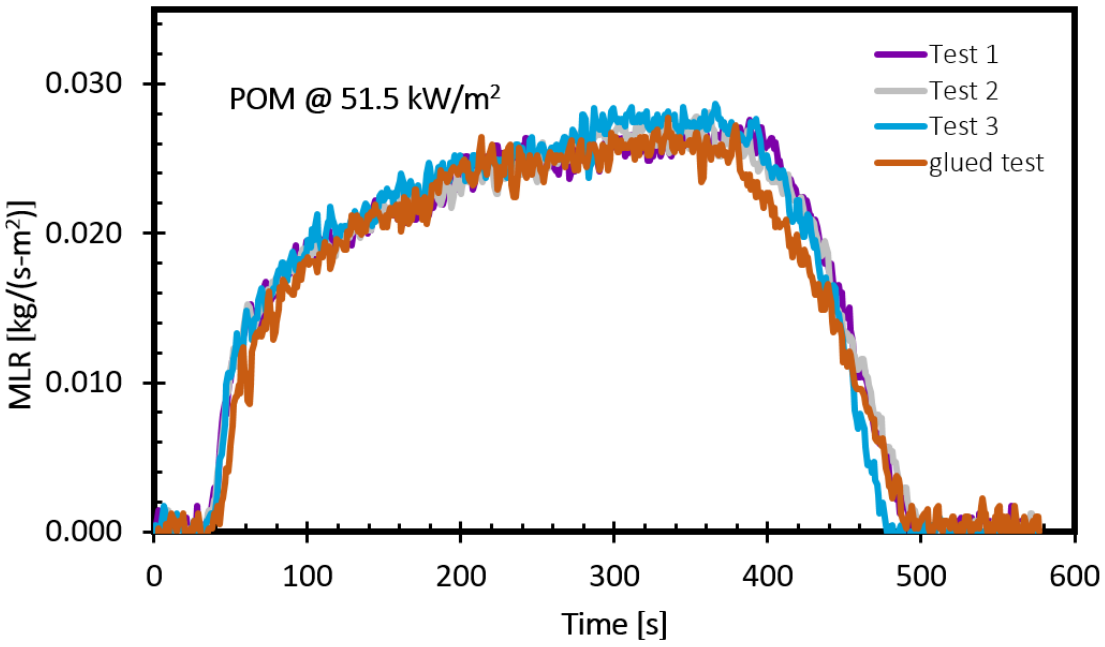

Figure A.2: Mass Loss Rate for POM at 51.5 kW/m^2

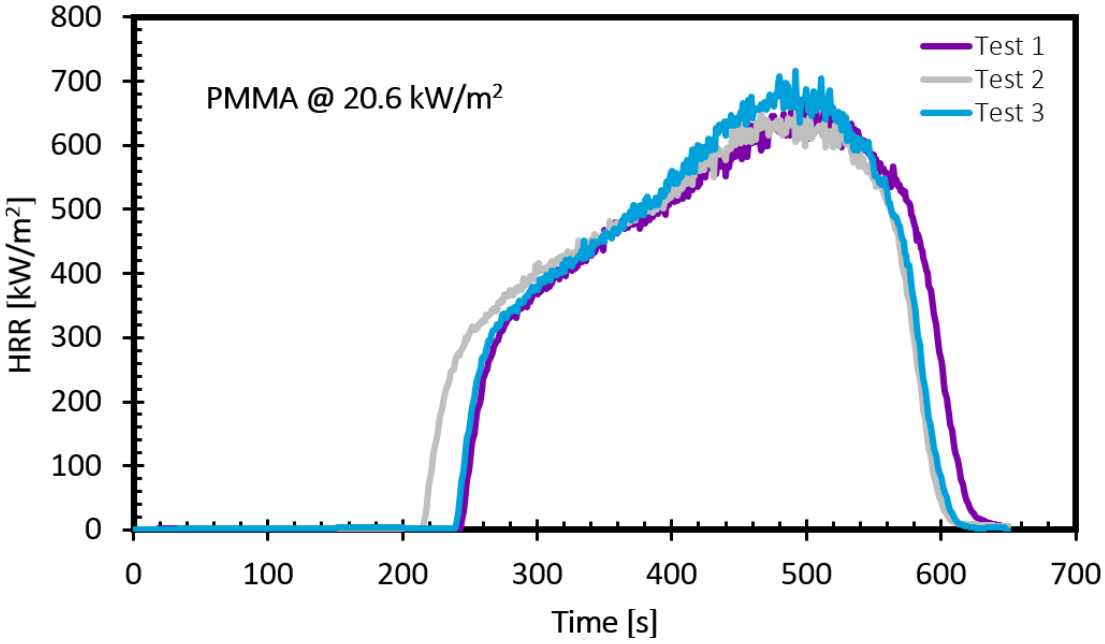

Figure A.3: Heat Release Rate for PMMA at 20.6 kW/m^2

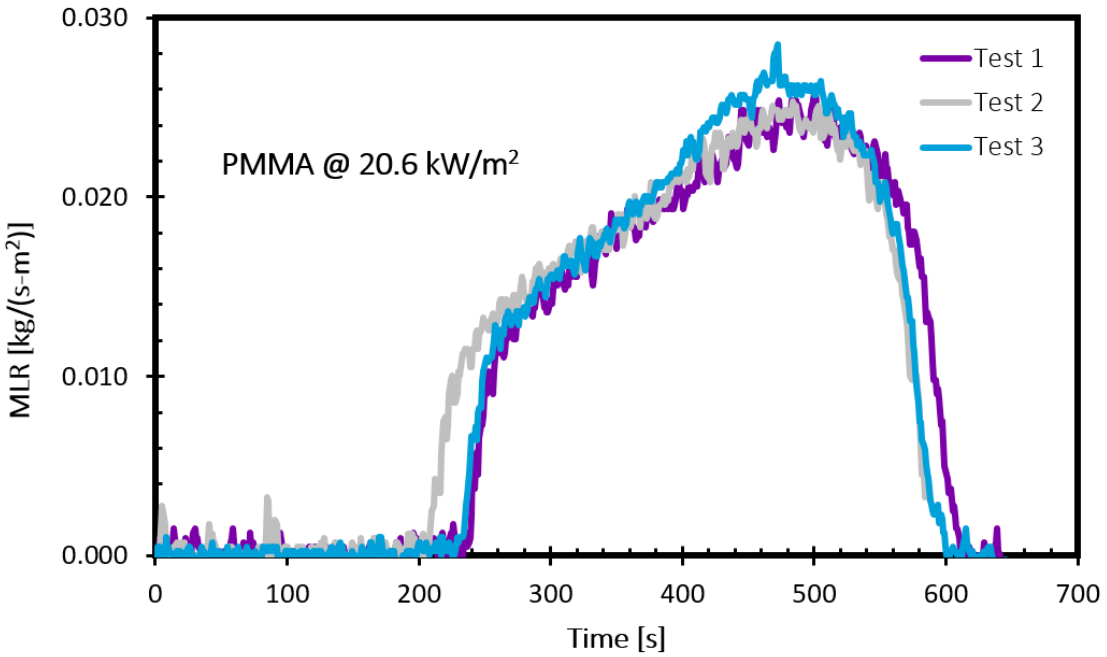

Figure A.4: Mass Loss Rate for PMMA at 20.6 kW/m^2

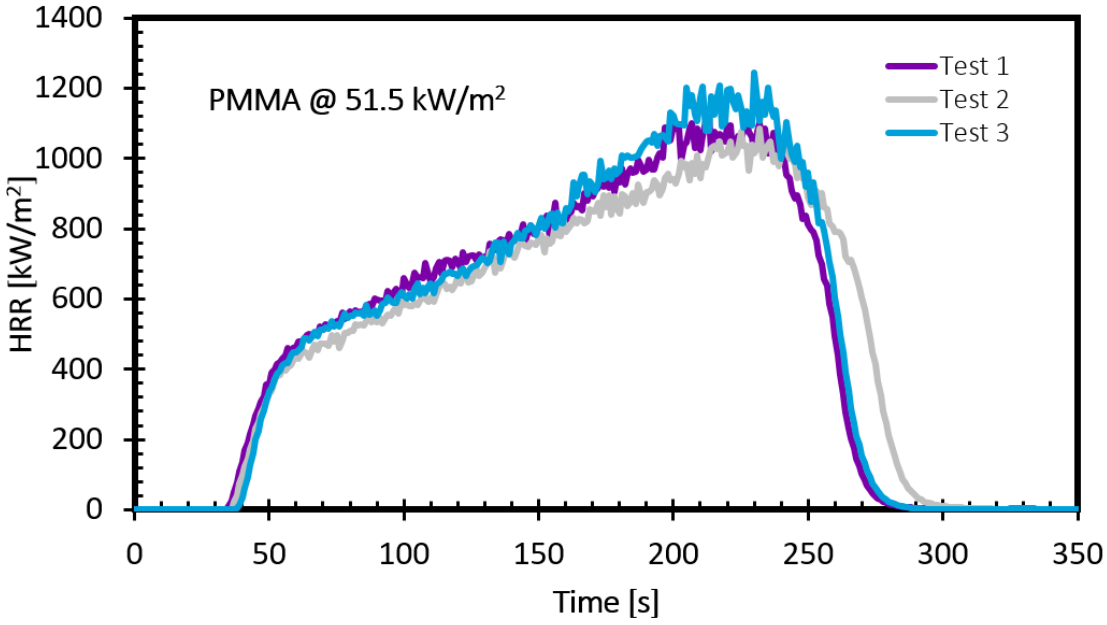

Figure A.5: Heat Release Rate for PMMA at 51.5 kW/m^2

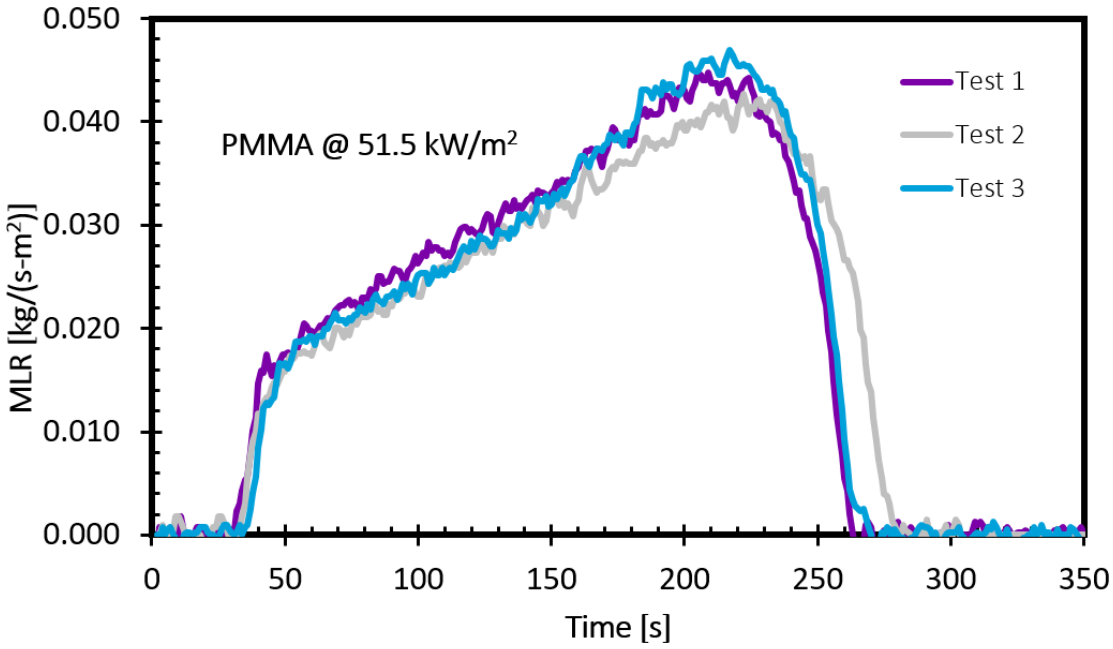

Figure A.6: Mass Loss Rate for PMMA at 51.5 kW/m^2

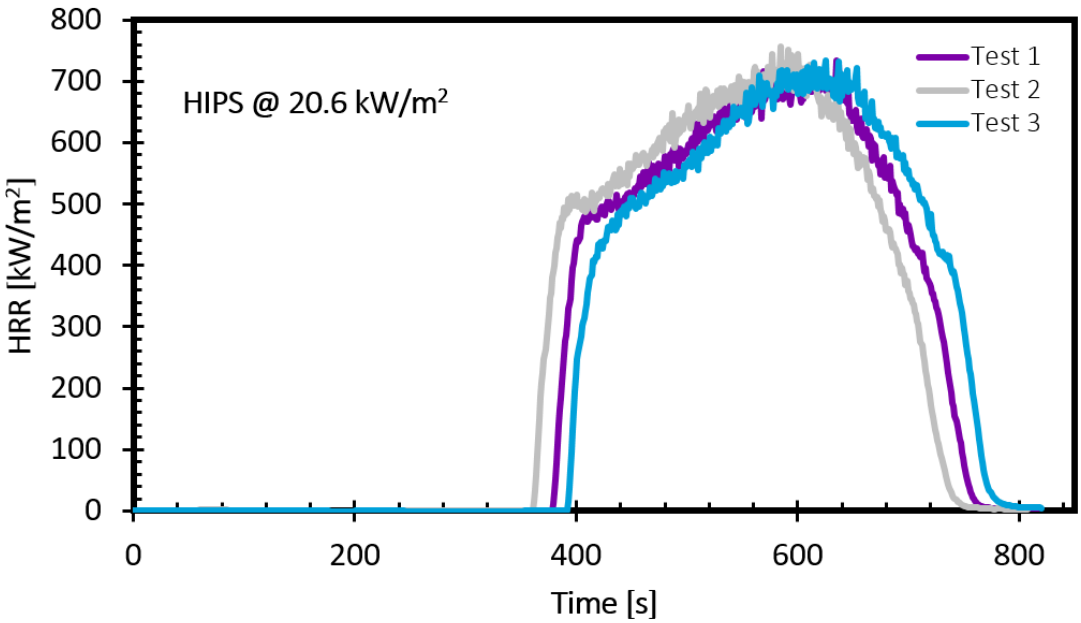

Figure A.7: Heat Release Rate for HIPS at 20.6 kW/m^2

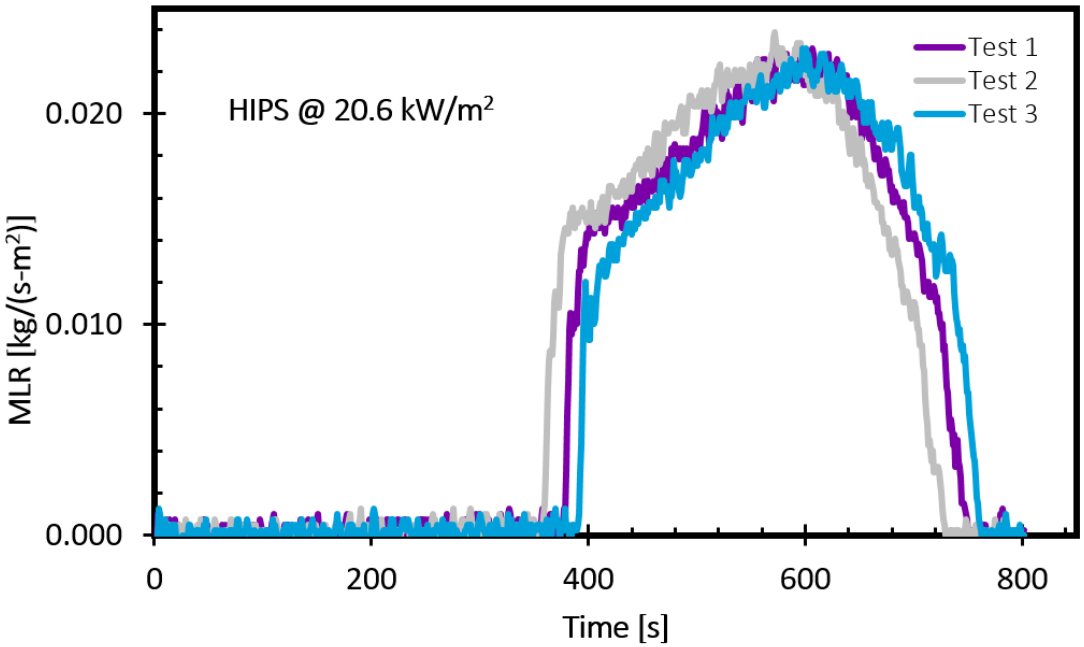

Figure A.8: Mass Loss Rate for HIPS at 20.6 kW/m^2

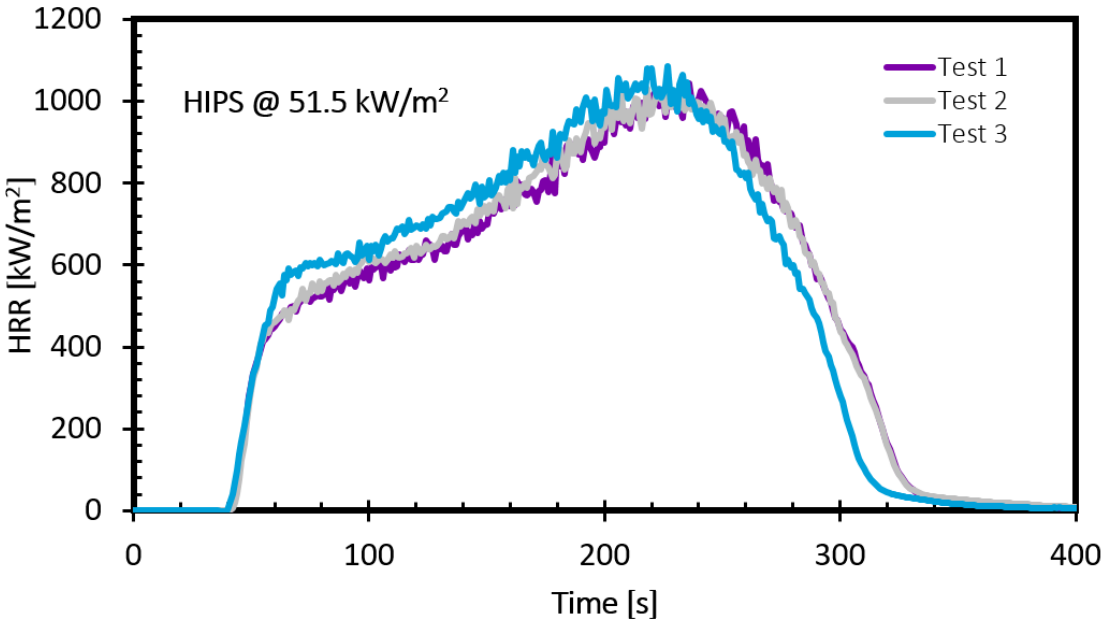

Figure A.9: Heat Release Rate for HIPS at 51.5 kW/m^2

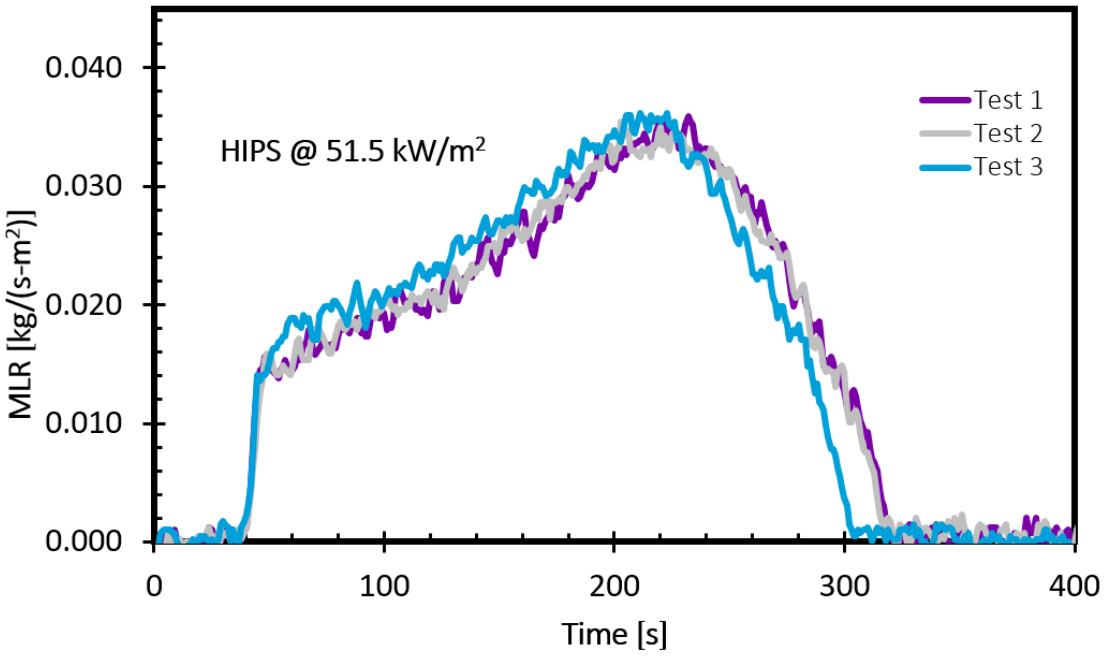

Figure A.10: Mass Loss Rate for HIPS at 51.5 kW/m^2

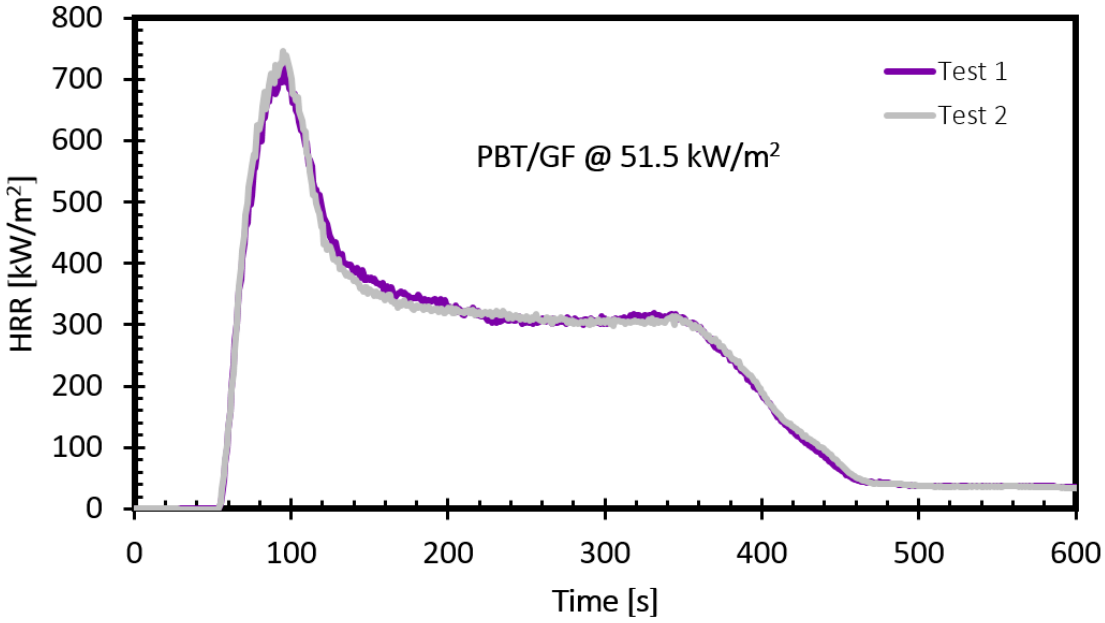

Figure A.11: Heat Release Rate for PBT/GF at 51.5 kW/m^2

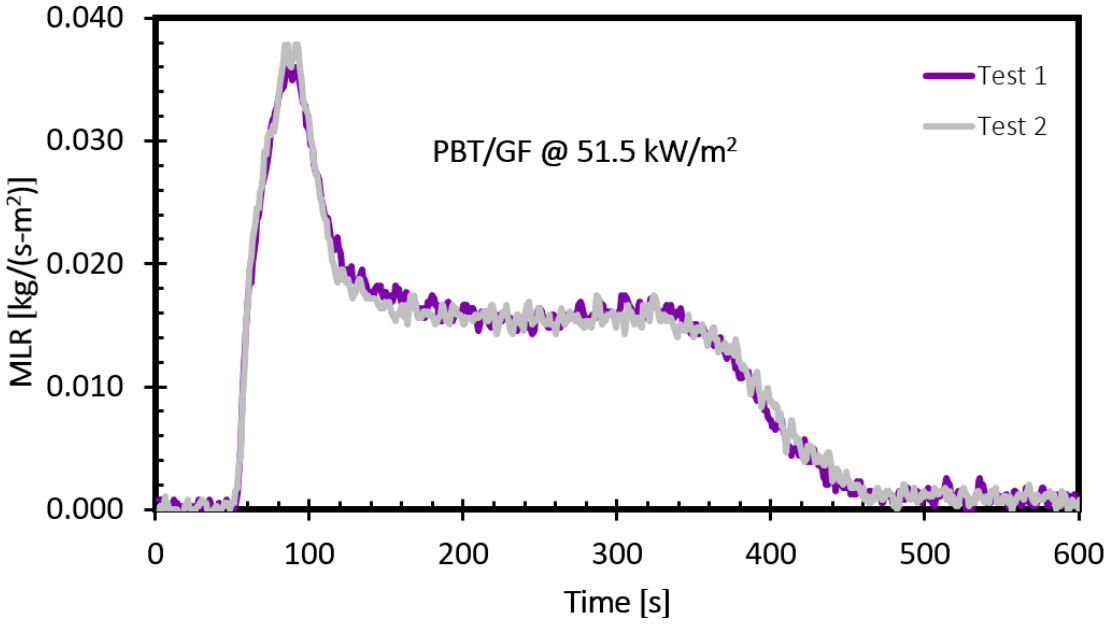

Figure A.12: Mass Loss Rate for PBT/GF at 51.5 kW/m^2

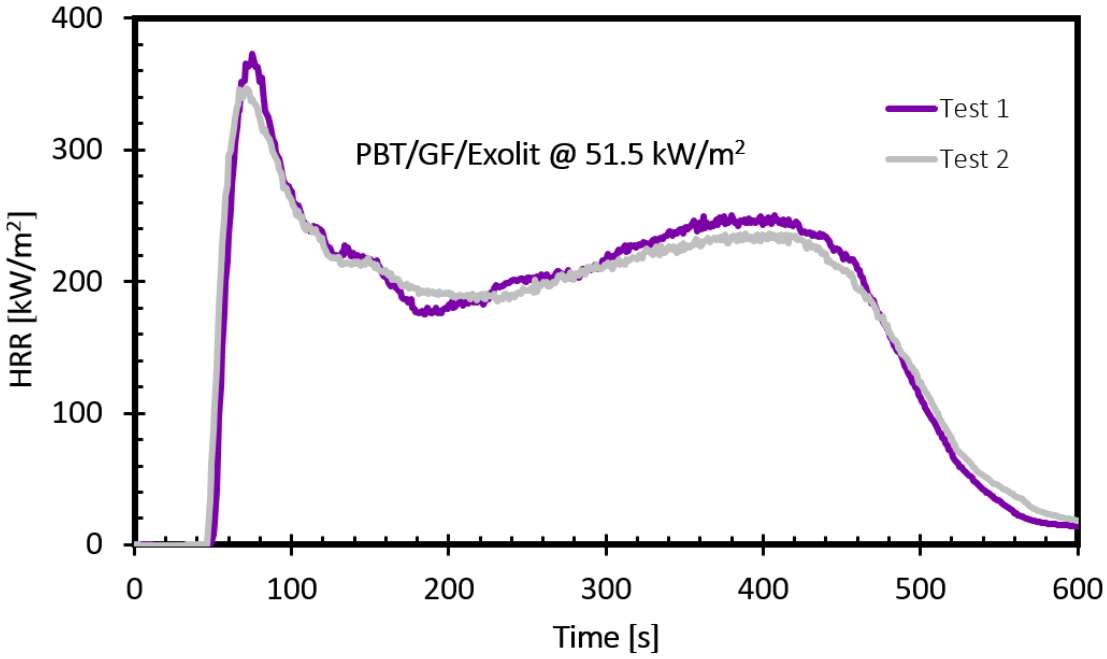

Figure A.13: Heat Release Rate for PBT/GF/Exolit at 51.5 kW/m^2

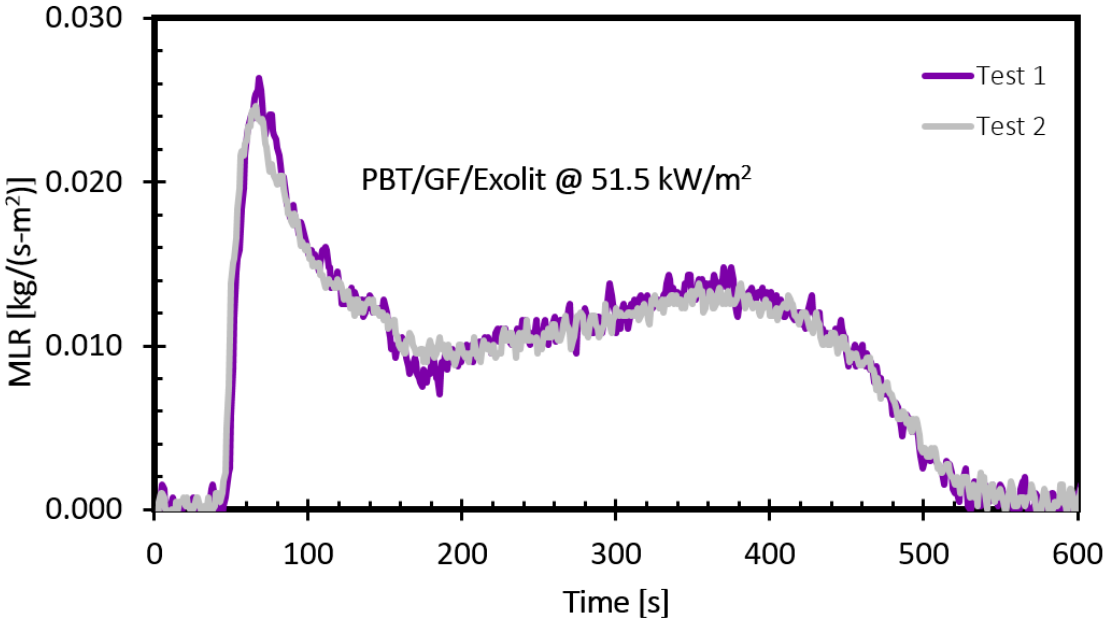

Figure A.14: Mass Loss Rate for PBT/GF/Exolit at 51.5 kW/m^2

A.2 Picture Timelines and Raw Heat Flux Graphs

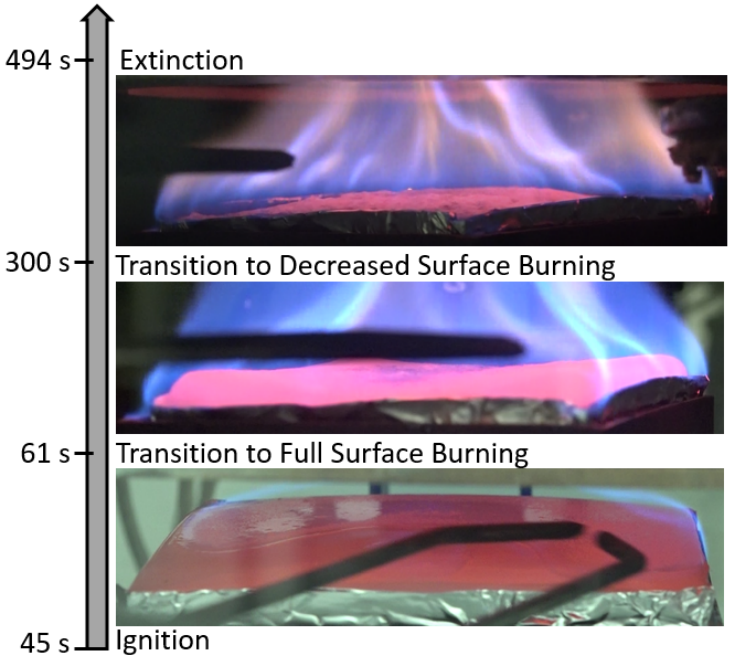

Figure A.15: Timeline of POM at 51.5 kW/m^2

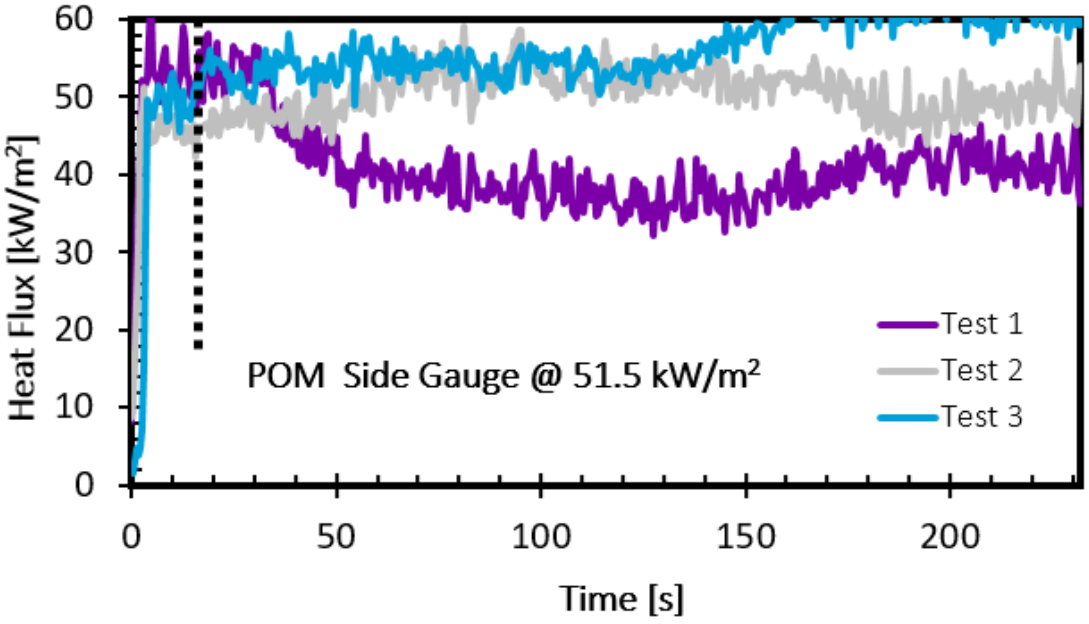

Figure A.16: Side Heat Flux of POM at 51.5 kW/m^2

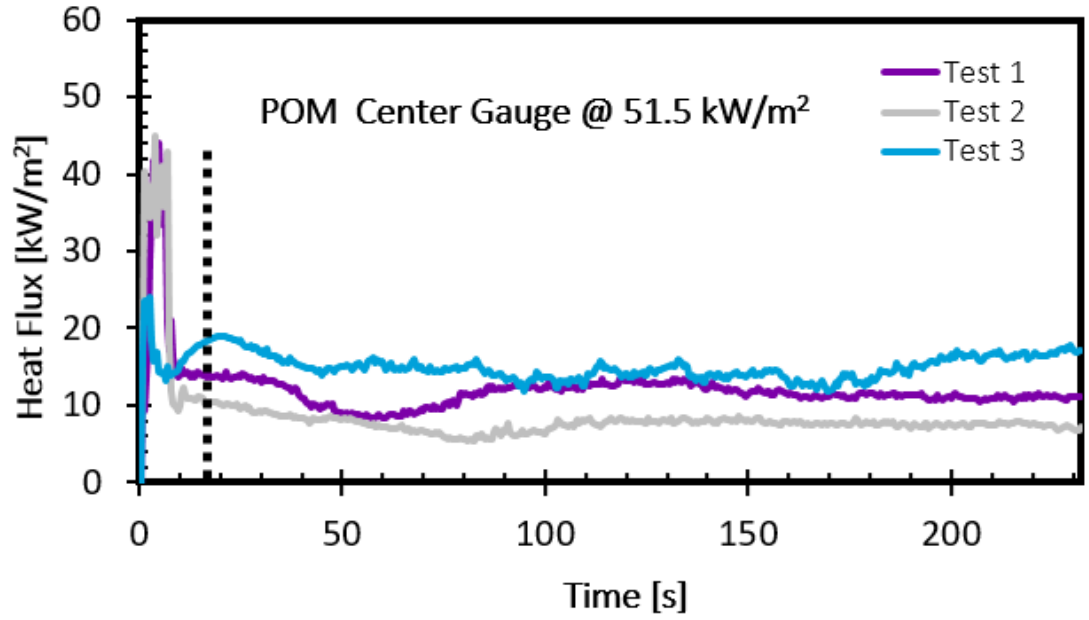

Figure A.17: Center Heat Flux of POM at 51.5 kW/m^2

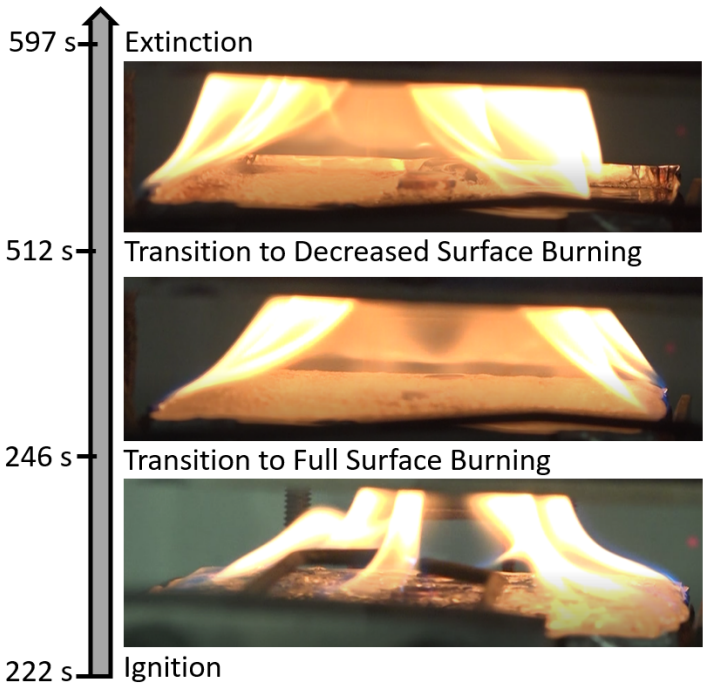

Figure A.18: Timeline of PMMA at 20.6 kW/m^2

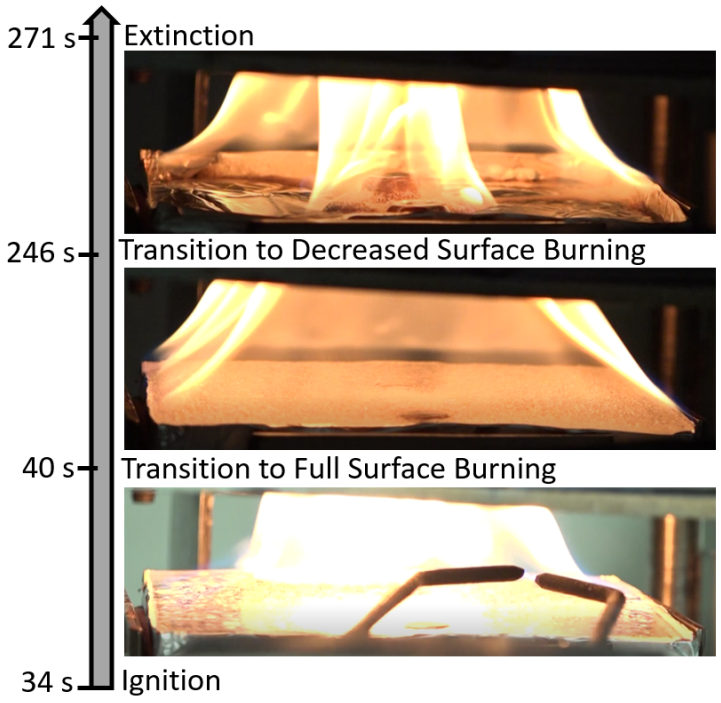

Figure A.19: Timeline of PMMA at 51.5 kW/m^2

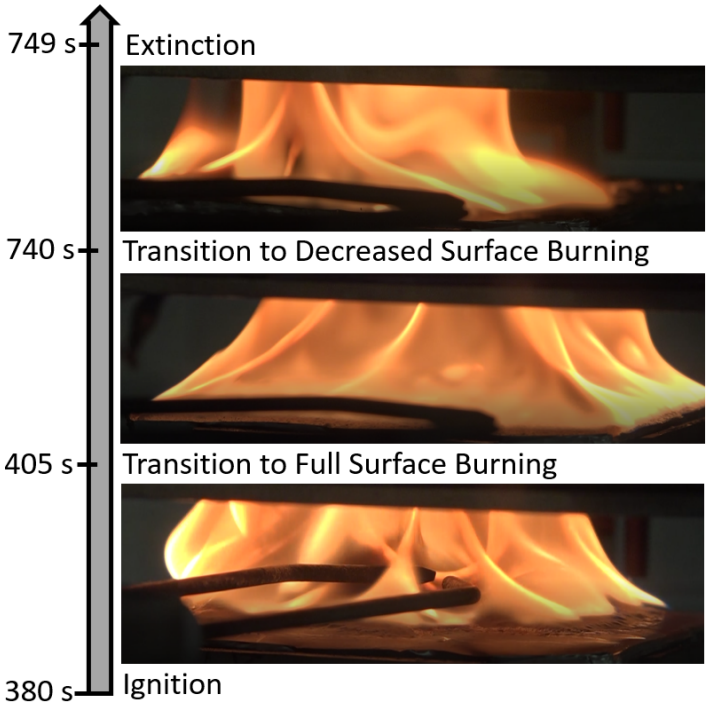

Figure A.20: Timeline of HIPS at 20.6 kW/m^2

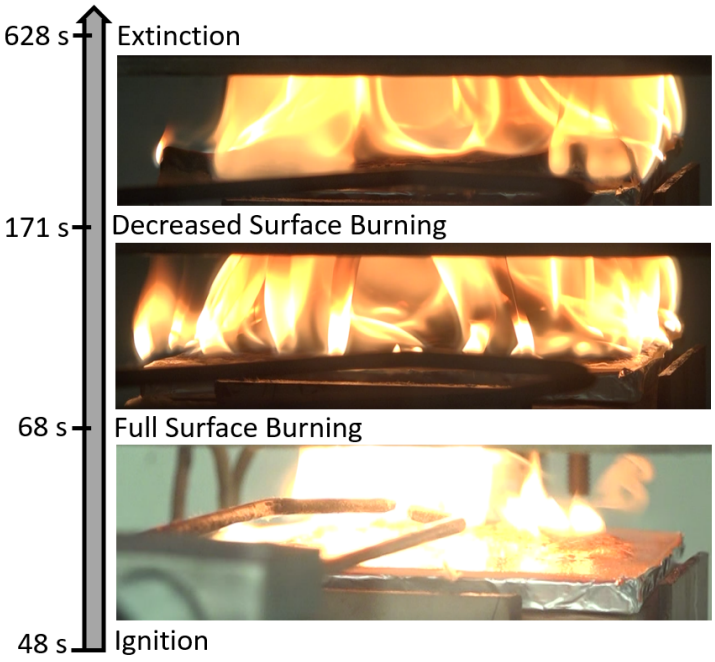

Figure A.21: Timeline of PBT/GF/Exolit at 51.5 kW/m^2

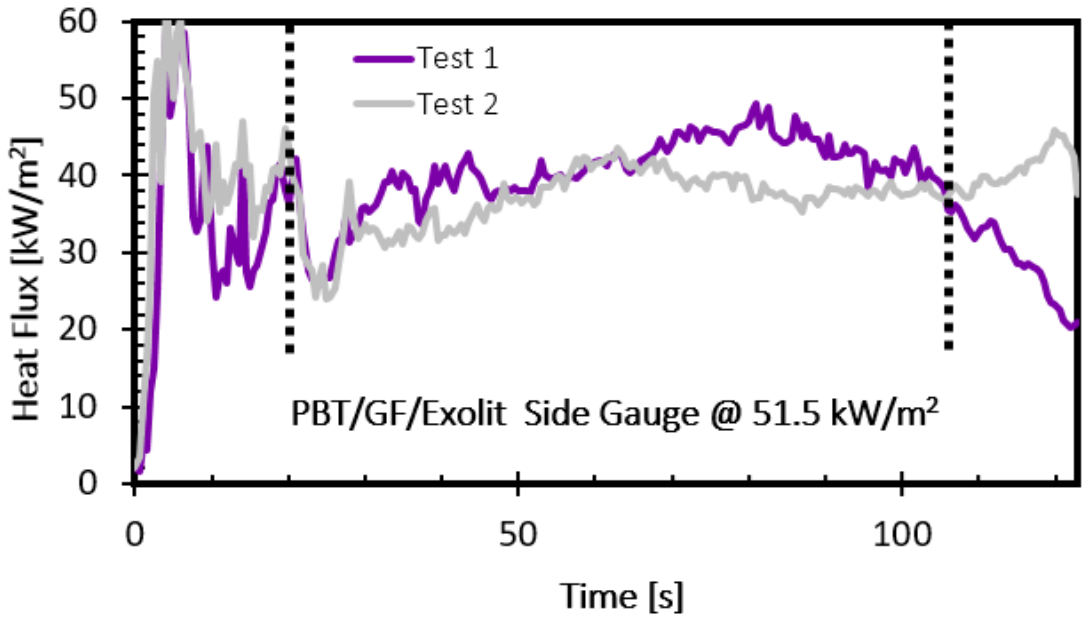

Figure A.22: Side Heat Flux of PBT/GF/Exolit at 51.5 kW/m^2

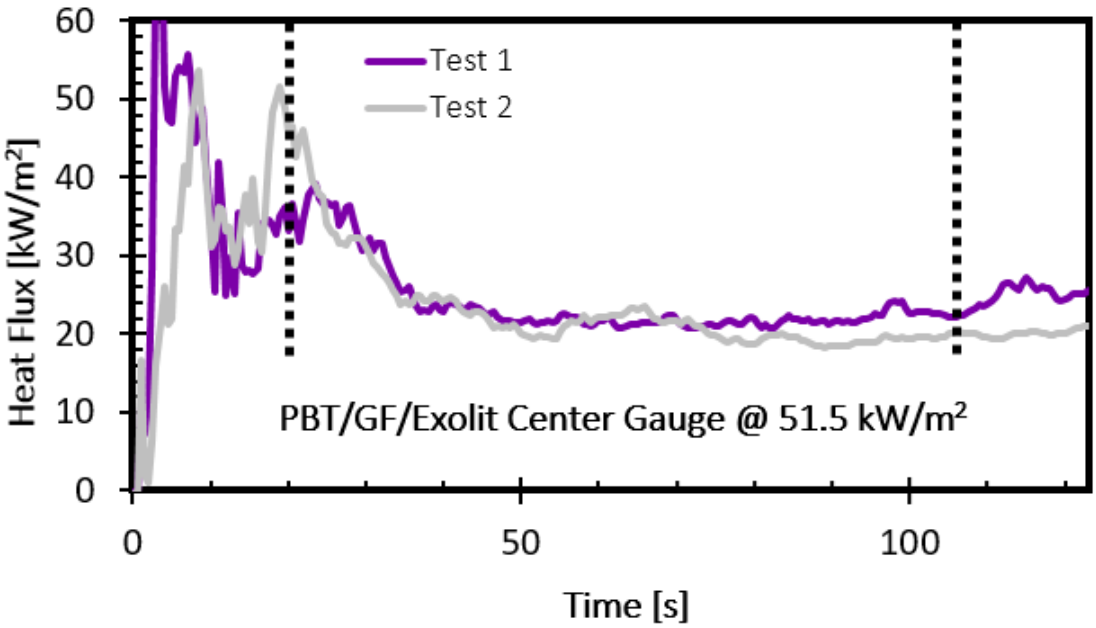

Figure A.23: Center Heat Flux of PBT/GF/Exolit at 51.5 kW/m^2

Bibliography

[1] Patricia A. Beaulieu and Nicholas A. Dembsey. Effect of oxygen on flame heat flux in horizontal and vertical orientations. *Fire Safety Journal*, 43:410–428, 2008.

[2] Issac T. Leventon, Jing Li, and Stanislav I. Stoliarov. A flame spread simulation based on a comprehensive solid pyrolysis model coupled with a detailed empirical flame structure representation. *Combustion and Flame*, 162:3884–3895, 2015.

[3] Germain Boyer. Fully coupled cfd simulation of the pyrolysis of non-charring polymers: A predictive approach. *Fire Safety Journal*, 2017.

[4] Issac T. Leventon, Kevin T. Korver, and Stanislav I. Stoliarov. A generalized model of flame to surface heat feedback for laminar wall flames. *Combustion and Flame*, 179:338–353, 2017.

[5] Theodore L. Bergman, Adrienne S. Lavine, Frank P. Incropera, and David P. Dewitt. *Fundamentals of Heat and Mass Transfer*. John Wiley Sons, Quincy, MA, seventh edition, 2011.

[6] Danny Hakim. Material at center of london fire will not be sold for high rises. *New York Times*, June 2017.

[7] Lauren Frayer. Reeling from its deadliest forest fire, portugal finds a villain: eucalyptus trees. *Los Angeles Times*, 2017.

[8] Vytenis Babrauskas and Richard D. Peacock. Heat release rate: The single most important variable in fire hazard. *Fire Safety Journal*, 18:255–272, 1992.

[9] Leonard Y. Cooper. A concept for estimating available safe egress time in fires. *Fire Safety Journal*, 5(2):135–144, 1983.

[10] Clayton Huggett. Estimation of rate of heat release by means of oxygen consumption measurements. *Fire and Materials*, 4(2):61–65, 1980.

[11] Vytenis Babrauskas. Development of the cone calorimeter - a bench-scale heat release rate apparatus based on oxygen consumption. *Combustion and Flame*, 8(2):81–95, 1984.

[12] ASTM International. Standard test method for heat and visible smoke release rates for materials and products using an oxygen consumption calorimeter. Technical Report E1354-16a, ASTM International, West Conshohocken, PA, January 2016.

[13] ASTM International. Standard test methods for measurement of material flammability using a fire propagation apparatus (fpa). Technical Report E2058-13a, ASTM International, West Conshohocken, PA, 2013.

[14] P Girods, N Bal, H Biteau, G Rein, and JL Torero. Comparison of pyrolysis behaviour results between the cone calorimeter and the fire propagation apparatus heat sources. pages 889–901, 2011.

[15] Brian T. Rhodes and James G. Quintiere. Burning rate and flame heat flux for pmma in a cone calorimeter. *Fire Safety Journal*, 26:221–240, 1996.

[16] Gregory Linteris, Lloyd Gewuerz, Kevin McGrattan, and Glenn Forney. Modeling solid sample burning. pages 625–636. International Association for Fire Science, 2005.

[17] Stanislav I Stoliarov and Richard E. Lyon. Thermo-kinetic model of burning for pyrolyzing materials. pages 1141–1152, 2009.

[18] Stanislav I. Stoliarov, Sean Crowley, Richard E. Lyon, and Gregory T. Linteris. Prediction of the burning rates of non-charring polymers. *Combustion and Flame*, 156:1068–1083, 2009.

[19] Florian Kempel, Bernhard Schartel, Gregory T. Linteris, Stanislav I. Stoliarov, Richard E. Lyon, Richard N. Walters, and Anja Hofmann. Prediction of the mass loss rate of polymer materials: Impact of residue formation. *Combustion and Flame*, 159:2974–2984, 2012.

[20] Ahmed Kacem, Maxime Mense, Pizzo Yannik, Germain Boyer, Sylvain Suard, Pascal Boulet, Gilles Parent, and Bernard Porterie. A fully coupled fluid/solid model for open air combustion of horizontally-oriented pmma samples. *Combustion and Flame*, 170:135–147, 2016.

[21] IRSN. Isis 4.0.0 physical modelling. Technical report, Institut de Radioprotection et de Sret Nuclaire, 2014.

[22] David Alibert, Mickael Coutin, Maxime Mense, Yannick Pizzo, and Bernard Porterie. Effect of oxygen concentration on the combustion of horizontally-oriented slabs of pmma. *Fire and Materials*, 2017.

[23] James G. Quintiere. *Fundamentals of Fire Phenomena*. John Wiley Sons, LTD, West Sussex, 2006.

[24] M. Janssens, J. Huczek, and A. Faw. Effect of specimen size on test results obtained in the cone calorimeter. Southwest Research Institute, 2008.

[25] Warren M. Rohsenow, James P. Hartnett, and Young I. Cho. *Handbook of Heat Transfer*. McGraw-Hill, 3rd edition, 1998.